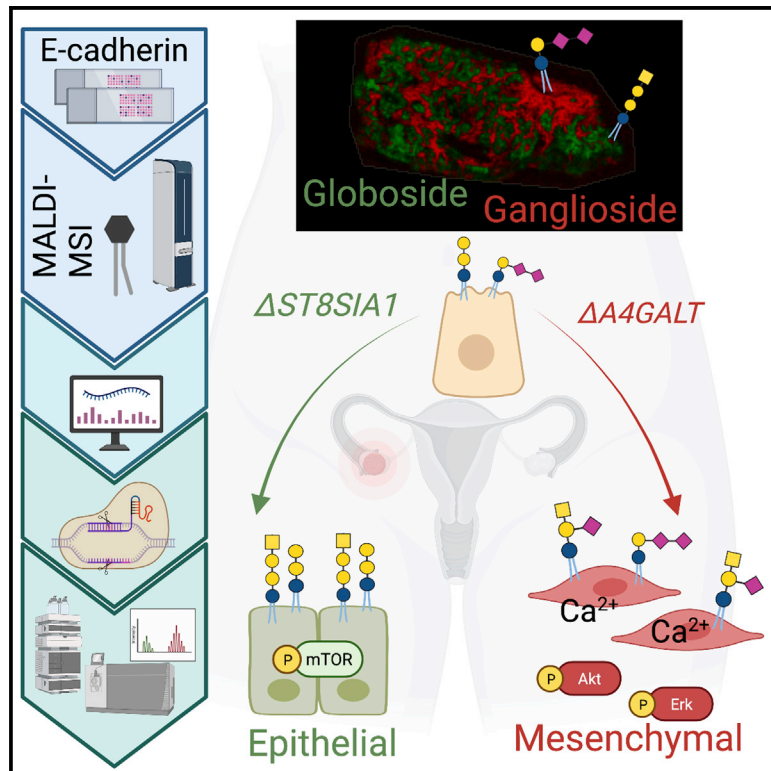# Glycosphingolipids are mediators of cancer plasticity through independent signaling pathways

Graphical abstract

Authors

Cécile Cumin, Yen-Lin Huang, Charlotte Rossdam, ..., Arun Everest-Dass, Viola Heinzelmann-Schwarz, Francis Jacob

Correspondence

a.everest-dass@griffith.edu.au (A.E.-D.), francis.jacob@unibas.ch (F.J.)

In brief

Cumin et al. propose that the glycosphingolipid composition on the cell surface of ovarian cancer cells determines the EMT state. Functional loss of key glycosyltransferases involved in glycolipid synthesis triggers the transition of cancer cells between epithelial and mesenchymal states, accompanied by intracellular signaling axes.

Highlights

- Ovarian cancer maintains the epithelial character throughout disease progression

- Glycolipid subtypes reflect epithelial-to-mesenchymal transition

- Sialylated glycolipids on mesenchymal cells may promote calcium-dependent signaling

CellPress

Cell Reports

Article

Glycosphingolipids are mediators of cancer plasticity through independent signaling pathways

Cécile Cumin,[1,2] Yen-Lin Huang,[1] Charlotte Rossdam,[3] Felix Ruoff,[4] Susana Posada Céspedes,[5] Ching-Yeu Liang,[1] Flavio C. Lombardo,[1] Ricardo Coelho,[1] Natalie Rimmer,[1] Martina Konantz,[6] Mónica Núñez López,[1] Shahidul Alam,[7] Alexander Schmidt,[8] Diego Calabrese,[1] Andre Fedier,[1] Tatjana Vlajnic,[9] Mark von Itzstein,[2] Markus Templin,[4] Falk F.R. Buettner,[3] Arun Everest-Dass,[2,*] Viola Heinzelmann-Schwarz,[1,10] and Francis Jacob[1,11,*]

[1]Ovarian Cancer Research, University Hospital Basel and University of Basel, Basel, Switzerland
[2]Institute for Glycomics, Griffith University, Gold Coast, QLD, Australia
[3]Institute of Clinical Biochemistry, Hannover Medical School, Hannover, Germany
[4]NMI Natural and Medical Sciences Institute at the University of Tübingen, Reutlingen, Germany
[5]Institute of Molecular and Clinical Ophthalmology Basel, Basel, Switzerland
[6]Stem Cells and Hematopoiesis, Department of Biomedicine, University Hospital Basel, University of Basel, Basel, Switzerland
[7]Centre for Organismal Studies, Heidelberg Universität, Heidelberg, Germany
[8]Biozentrum University of Basel, Basel, Switzerland
[9]Institute of Pathology, Kantonsspital Graubünden, Chur, Switzerland
[10]Department of Gynecology and Gynecological Oncology, Hospital for Women, University Hospital Basel, Switzerland
[11]Lead contact
*Correspondence: a.everest-dass@griffith.edu.au (A.E.-D.), francis.jacob@unibas.ch (F.J.)
https://doi.org/10.1016/j.celrep.2022.111181

SUMMARY

The molecular repertoire promoting cancer cell plasticity is not fully elucidated. Here, we propose that glycosphingolipids (GSLs), specifically the globo and ganglio series, correlate and promote the transition between epithelial and mesenchymal cells. The epithelial character of ovarian cancer remains stable throughout disease progression, and spatial glycosphingolipidomics reveals elevated globosides in the tumor compartment compared with the ganglioside-rich stroma. CRISPR-Cas9 knockin mediated truncation of endogenous E-cadherin induces epithelial-to-mesenchymal transition (EMT) and decreases globosides. The transcriptomics analysis identifies the ganglioside-synthesizing enzyme *ST8SIA1* to be consistently elevated in mesenchymal-like samples, predicting poor outcome. Subsequent deletion of *ST8SIA1* induces epithelial cell features through mTOR^{S2448} phosphorylation, whereas loss of globosides in *ΔA4GALT* cells, resulting in EMT, is accompanied by increased ERK$^{Y202/T204}$ and AKT^{S124}. The GSL composition dynamics corroborate cancer cell plasticity, and further evidence suggests that mesenchymal cells are maintained through ganglioside-dependent, calcium-mediated mechanisms.

INTRODUCTION

The human glycome consists of free oligosaccharides and glycans linked to proteins and lipids forming the glycocalyx (Schjoldager et al., 2020). Glycosphingolipids (GSLs) are anchored to the outer leaflet of the cell plasma membrane via their ceramide backbone and are primarily separated into globo, ganglio, and (neo) lacto series (Schnaar and Kinoshita, 2015). Gangliosides are sialylated GSLs and have been studied in clinical trials assessing vaccination and in antibody-based therapy and have also been studied as ligands for CAR-T cells (Mereiter et al., 2019), with promising outcomes for the anti-GD2 (disialylated ganglioside) monoclonal antibody (Federico et al., 2017; Yu et al., 2010). Targeting GD2 in neuroblastoma, osteosarcoma, and small-cell lung cancer is further supported by a recent study showing synergy in combination with anti-CD47 treatment, significantly reducing the tumor burden and extending survival (Theruvath et al., 2022). There is increasing evidence showing

that GSLs are a class of biomolecules involved in multiple pathophysiological processes, including human malignancies (Cumin et al., 2021). One hallmark of cancer is the ability of cancer cells to undergo plastic and molecular differentiation, also referred to as epithelial-to-mesenchymal transition (EMT). This cellular process, by which cancer cells lose their epithelial characteristics to acquire mesenchymal features, has been implicated in tumor initiation, progression, stemness, cell metastasis, and drug resistance (Pastushenko and Blanpain, 2019). Although EMT is nowadays subdivided into multiple transition states characterized by co-expression of epithelial and mesenchymal markers, it is becoming evident that cells reverting to hybrid, intermediate, or incomplete states display the highest plasticity and have been associated with predicting resistance to therapy and poor survival in multiple cancer types (George et al., 2017; Schliekelman et al., 2015; Yamashita et al., 2018). However, experimental transition or rescue of cells that underwent full or partial EMT seems to be rather difficult
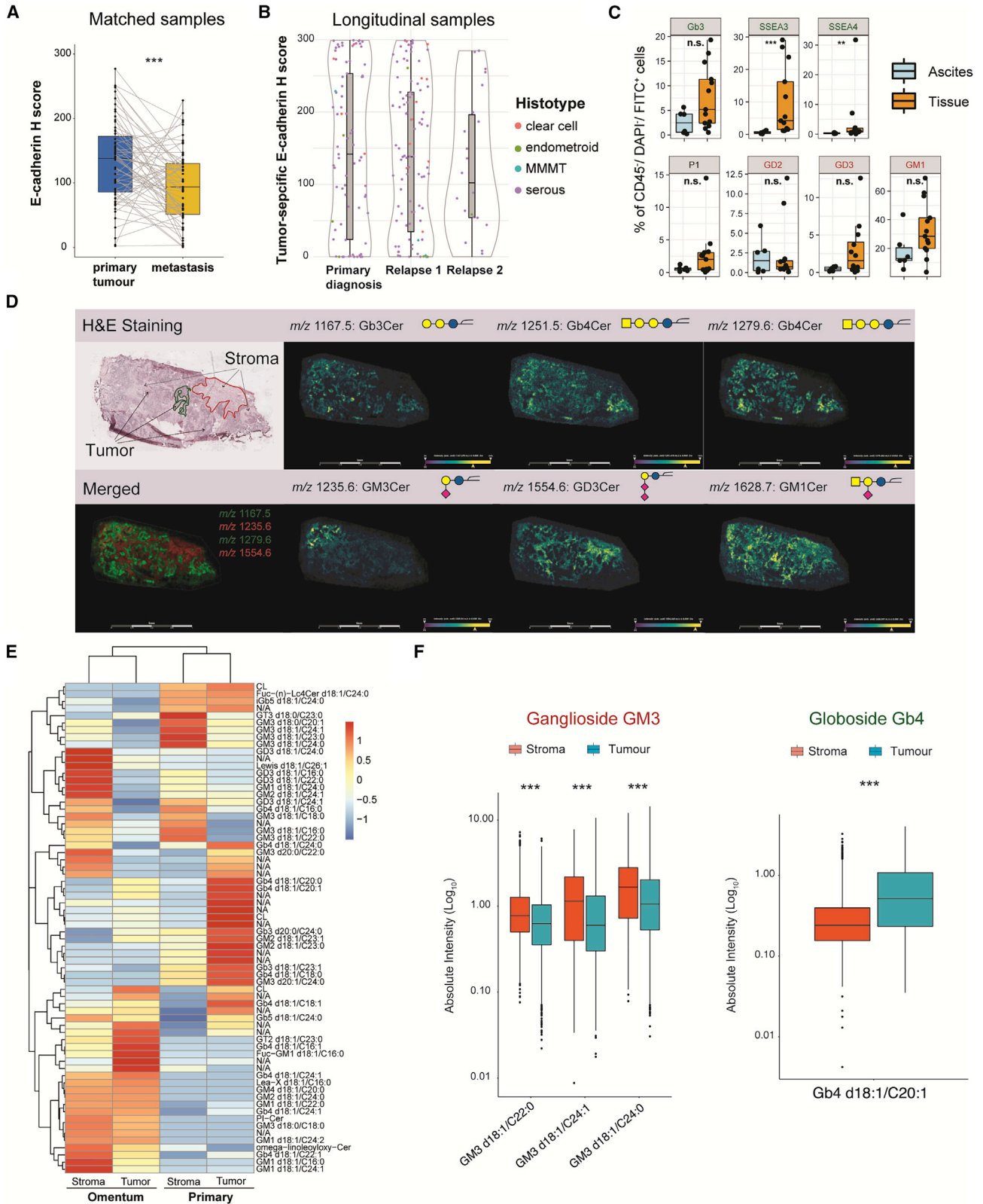
(legend on next page)

(Jacob et al., 2018; Pastushenko et al., 2018), suggesting that reversible EMT (mesenchymal-to-epithelial transition [MET]) is a rare event, questioning the metastatic outgrowth of mesenchymal cells at distant sites. This is supported by recent work showing that EMT and MET are promoted by distinct cellular processes in lung cancer, characterized by downregulation of pEGFR/pS6 and pAMPK signaling, respectively (Karacosta et al., 2019). Interestingly, TCGA cancer types can be classified into four major categories of EMT based on specific gene expression signatures, with ovarian cancer (OC), among others, covering the full spectrum of EMT (Tan et al., 2014). Cancer EMT-associated alteration of GSLs has been reported earlier by Liang et al. (2013). CD44^{high}/CD24^{low} breast cancer stem cell-like cells revealed elevated gangliosides accompanied by drastically reduced Fuc-(n)Lc4Cer and the globoside Gb3 (Liang et al., 2013). In agreement with these observations, we also previously demonstrated that functional loss of globosides upon genetic deletion of *A4GALT* induces EMT in intermediate epithelial OC cells, suggesting that globosides are involved in maintenance of epithelial-like characteristics (Jacob et al., 2018). The dynamic balance between gangliosides and globosides also appeared in mesenchymal-like pancreatic cancer cells compared with their epithelial counterparts (Zhang et al., 2020). Pattabiraman et al. (2016) have reported *CDH1* promoter activation in human mammary epithelial cells after treatment with the multimeric protein complex cholera toxin from *Vibrio cholerae*, known to bind a major ganglioside-type GSL, GM1. The current literature points toward involvement of GSLs during EMT but is uncertain regarding MET. In this study, we functionally demonstrate that specific GSLs define epithelial and mesenchymal cancer cells and promote EMT or MET through distinct and independent signaling mechanisms.

RESULTS

The epithelial-like phenotype of OC is maintained throughout disease progression and shows enrichment of globosides

Intra-abdominal dissemination requires disaggregation of solid tumor tissue to reach the peritoneal cavity and distant sites. Through the transcoelomic route, cancer cells generate metastatic lesions using cell-ECM adhesion molecules, allowing adherence to organs within the peritoneal cavity (Huang et al., 2020; Iwanicki et al., 2011; Sawada et al., 2008). We first investigated the intra-individual heterogeneity of E-cadherin across a cohort of (1) primary and matched metastatic tumor sites in 135

individuals with OC in total including 63 individuals with matched sites (Tables S1 and S2) and (2) longitudinal (n = 54 individuals with OC with tissue obtained at primary diagnosis, first, and second relapse; Table S2) using immunohistochemistry combined with quantitative tissue analysis (Figure S1A). Despite a significant drop of tumor-specific E-cadherin expression at the metastatic site at the time of debulking surgery, E-cadherin remained present at both sites, with strong expression in the tumor compartment compared with the stroma (Figures 1A, S1A, and S1B). We found that tissue samples derived from primary tubo-ovarian sites revealed the highest E-cadherin expression in high-grade OC samples, whereas a gradual decrease of E-cadherin was observed in metastatic tissue samples with dependencies on FIGO stage and histology (Figures 1A, 1B, and S1C). Further investigation of the longitudinal cohort revealed only marginally altered E-cadherin expression throughout the course of the disease (Figures 1 and S1D). The expression of E-cadherin in almost all investigated tissue samples supports the hypothesis that the epithelial component in the majority of OC samples remains present throughout the different stages of the disease.

Considering the high abundance of epithelial cancer cells, we next performed flow cytometry on CD45$^-$ cells derived from enzymatically dissociated tissue and ascites samples from individuals with high-grade serous OC (slow frozen, n = 19). We found a large spectrum of GSL positivity, with globosides being elevated in the tissue samples compared with the ascites (Figures 1C, S2A, and S2B), supporting our hypothesis that globosides are abundant in epithelial-like OC. To spatially determine total GSL expression in human OC tissue, we utilized negative-mode MALDI-mass spectrometry imaging (MSI) (Colsch and Woods, 2010; Ermini et al., 2017). The powerful feature of MALDI-MSI is non-targeted registration of analytes in a spatially resolved manner to assign and distinguish various GSLs. We established a protocol to detect GSLs [M-H]$^-$ species in snap-frozen tissues (n = 17) and identified a total of 39 GSL *m/z* ion signals with 19 GSL-related *m/z* ions annotated previously in the literature (Bien et al., 2020; Chang et al., 1997; Ikeda et al., 2008; Ruh et al., 2013; Säljö et al., 2017; Table S3). We also identified 20 isomeric GSLs because of their fatty acid chains (Table S3). The MALDI-MSI analysis of OC tissue sections revealed high Gb3Cer and Gb4Cer expression in the tumor region with a similar distribution pattern. In contrast, several ganglioside lipoforms (GD3Cer, GM3Cer, and GM1Cer) were elevated in the stroma (Figure 1D). All gangliosides detected had similar spatial distribution with varying absolute intensity because of different

Figure 1. E-cadherin and globosides are elevated in primary and matched metastatic tissue samples derived from individuals with OC

(A) Tumor-specific E-cadherin expression (H score) in primary and matched (gray line) metastatic tissue, evaluated by IHC and analyzed using HALO.

(B) H score for tumor cells comparing primary diagnosis and first (relapse 1) and second disease recurrence (relapse 2), stratified by cancer histotype.

(C) Flow cytometry-determined GSL in ascites and tumor tissue samples derived from individuals with high-grade serous OC (n = 19 samples). Shown is a boxplot with the percentage of CD45$^-$/DAPI$^-$/ fluorescein isothiocyanate (FITC)$^+$ cells.

(D) Spatial distribution of Gb3Cer, Gb4Cer, GM3Cer, GM1Cer, and GD3Cer using MALDI-MS imaging from an omentum tumor with the corresponding H&E staining.

(E) Unsupervised hierarchical clustering and heatmap representing GSL expression among primary tumor and metastatic (omentum) sites, separated into tumor and stroma compartments.

(F) Quantification of overall globosides (Gb4Cer) and gangliosides (GM3Cer) detected using MALDI-MS imaging in 17 fresh-frozen samples in the tumor and stroma region. N/A, (glyco)lipid not confirmed by the literature.

Statistical analysis by paired or unpaired Student's t test; n.s., not significant; *p < 0.05, **p < 0.01, ***p < 0.001. See also Figures S1 and S2 and Tables S1 and S2.
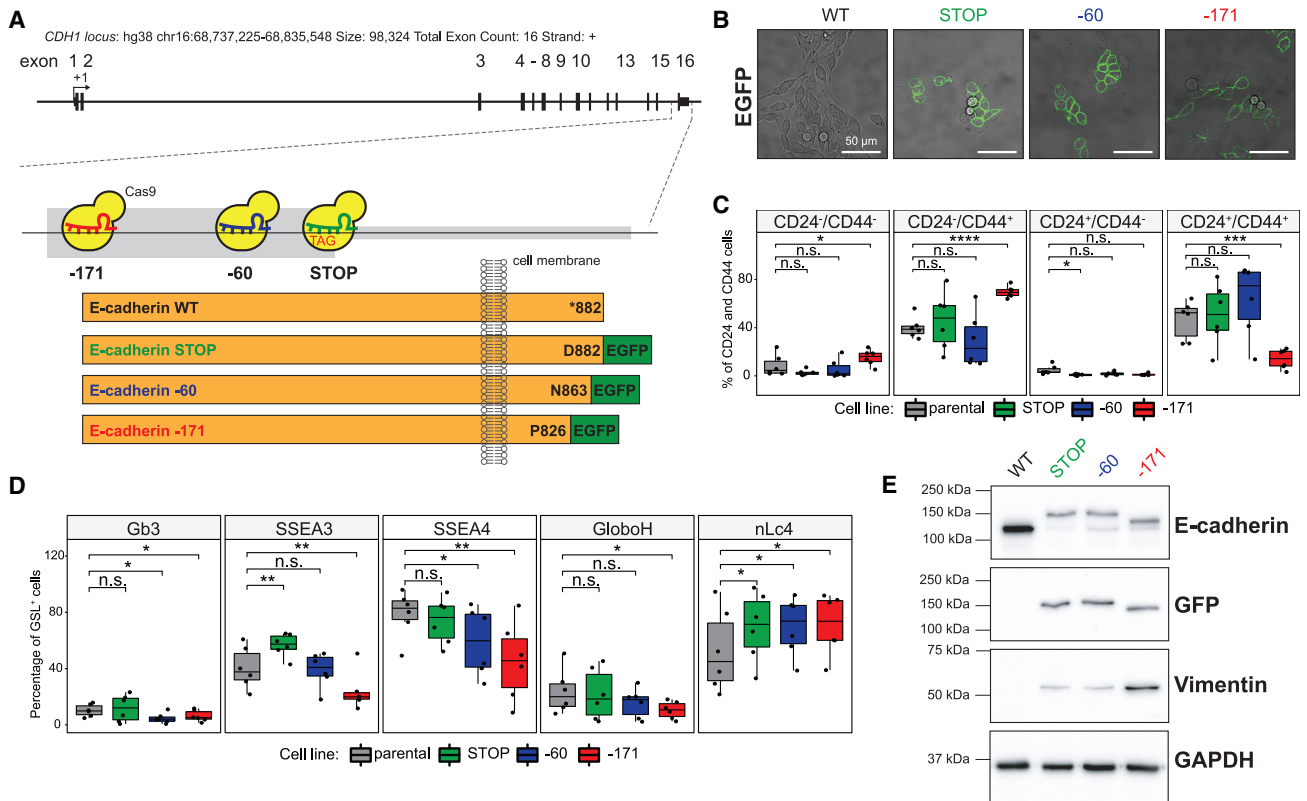
Figure 2. C-terminal E-cadherin truncation alters GSL abundance and coincides with an EMT-associated phenotype *in vitro*
(A) Schematic representation of the gene editing strategy.
(B) Corresponding live-cell immunofluorescence of wild-type and EGFP E-cadherin-tagged OC cells after cell sorting. Scale bar, 50 μm.
(C) Fluorescence-activated cell sorting (FACS) analysis of cancer stem cell-like marker CD24 and CD44 alteration with increasing truncation of the E-cadherin cytoplasmic tail (n = 6 experiments).
(D) FACS analysis shows reduction of the globosides Gb3, SSEA3, SSEA4, and Globo H in *CDH1*-edited BG1 cells (n = 6 experiments).
(E) Verification on the protein level using western blotting, showing a shift of molecular weight upon EGFP insertion and increase of Vimentin with enlarged truncation of the E-cadherin cytoplasmic tail.
Student's t test; *p < 0.05, **p < 0.01, ***p < 0.001. See also Figure S3.

fatty acid lengths. To quantify the spatial expression of GSLs in the samples investigated, we extracted the signal intensity for each pixel (50 μm) from pre-defined tissue regions of interest similar in size (Figures S2C and S2D). Combined analysis revealed elevated globosides in the tumor region, whereas the stroma was dominated by the presence of various gangliosides (Figures 1E and 1F). The combined results of tumor-specific E-cadherin together with our flow cytometry approach and spatial glycosphingolipidomics in tissue samples from affected individuals indicate that globosides are elevated in epithelial-like OC, whereas gangliosides are preferentially enriched in mesenchymal-like cells.

Endogenous truncation of the E-cadherin cytoplasmic tail results in EMT accompanied by reduced globosides

The epithelial cell surface protein E-cadherin has been suggested to functionally act in controlling tumor cell metastasis (Na et al., 2020); for example, binding of β-catenin to the E-cadherin cytotail maintains homophilic cell-cell adhesion (Auersperg et al., 1999; Tian et al., 2011). Here, dysregulation

of β-catenin may elevate nuclear β-catenin levels and lead to activation of Wnt-related targets, including Slug, ZEB1, and MMP-7, promoting features of EMT (Song et al., 2019). Thus, we hypothesized that the stepwise truncation of the endogenous E-cadherin catalytic domain may consequently alter globoside expression, usually enriched in epithelial-like cancer cells. We applied a modified endogenous CRISPR-Cas9-mediated knockin strategy (He et al., 2016) to insert the EGFP-encoding DNA sequence at three distinct genomic loci (E-cadherin STOP, −60, and −171) in an epithelial OC cell line (Figure 2A). Downstream flow cytometry-based enrichment of EGFP+ cells (Figures 2B and S3A) and insertion of EGFP at targeted regions was confirmed at the genomic locus (Figure S3B). Downstream flow cytometry revealed an increase in the CD24^low CD44^high (mesenchymal-like) signature in E-cadherin-171 compared with wild-type cells (Figures 2C and S3C). Regarding GSLs, the globosides SSEA3, SSEA4, and Globo H were reduced in E-cadherin-171 cells compared with the remaining cell lines (Figures 2D, S3D, and S3E). We also noticed elevated expression of the mesenchymal marker Vimentin in *CDH1*-edited cells,

with a gradual increase toward −171 (Figures 2E and S3G). Colony formation confirmed that BG1 cells underwent EMT upon genetic truncation of the E-cadherin cytoplasmic tail, as shown by reduced anchorage-(in)dependent growth (Figure S3F). These data suggest that truncation of E-Cadherin leads to a reduction of globosides on epithelial OC cells, supporting the interplay between globosides and cellular and molecular epithelial characteristics.

Mesenchymal-like cancer cells are enriched in ganglioside-encoding glycosyltransferases

Considering the generally low abundance of mesenchymal-like OC cells being E-cadherin low or negative, we hypothesized that cells enriched in ganglioside-synthesizing glycosyltransferases express an EMT-like gene expression signature. We investigated whether MET can be induced by modulating respective glycosyltransferase-encoding genes involved in GSL synthesis. To identify the most promising glycosyltransferase, we assessed publicly available datasets and applied them to the previously described EMT score (Tan et al., 2014). We observed that elevated expression of several ganglioside glycosyltransferase-encoding genes (e.g., ST8SIA1, ST3GAL2, ST3GAL3, and B4GALNT1) coincides with mesenchymal marker expression of VIM and FN1 (Figure S4). This pattern was consistent among the epithelial (E), intermediate E (IE), intermediate mesenchymal (IM), and mesenchymal (M) states in five large transcriptomic datasets derived from OC tissue, showing that EMT-associated genes such as CDH1 and VIM are significantly up- and down-regulated in the E and M state, respectively (Figure 3A, S5A, and S5B). Aligned with our recent findings, the glycosyltransferase-encoding gene A4GALT was elevated in OC samples with E features (Jacob et al., 2018). In contrast, high ST8SIA1 correlates with low CDH1 and high VIM expression (Figure 3A). EMT has also been associated with disease outcome in various cancer types (Chen et al., 2016; Gooding and Schiemann, 2020; Tan et al., 2014); thus, we next assessed the CuratedOvarianData package comprising a large OC gene expression database with individual survival information (Ganzfried et al., 2013). As expected, CDH1 (p = 0.0002) and A4GALT (p = 0.0786) presented a hazard ratio of 0.90 and 0.92, respectively. In contrast, elevated expression of VIM (p = 0.0085) and ST8SIA1 (p = 0.0111) with a hazard ratio of 1.08 predicted poor overall survival (Figure 3B).

The ST8SIA1 gene encodes the key enzyme in the synthesis of gangliosides GD3 and GT3 (Merrill, 2011), according to the KEGG pathway database. Based on transcriptomics data, we selected ST8SIA1 as the most promising target gene to functionally induce MET in OC cells. According to EMT marker expression (Figure 3C) and previous publications, we used SKOV3, which is defined as an IM cell line (Dunfield et al., 2002; Huang et al., 2013), as well as TOV112D and SKOV3ip as M and E cell lines, respectively. We did not find an association of the previously proposed EMT score (Tan et al., 2014) with the suitability score of the serous OC histotype (Domcke et al., 2013) when analyzing the transcriptome of the Cancer Cell Line Encyclopedia (CCLE), indicating that different EMT states are unlikely to be associated with histotypes in OC cell lines (Figure S5C). We then homozygously deleted ST8SIA1 in SKOV3 using our

paired single guide RNA (sgRNA) CRISPR-Cas9 approach (Alam et al., 2017; Jacob et al., 2018), targeting the first exon of ST8SIA1 encoding the transcription and translation start site, resulting in a 1,094-bp genomic deletion on chr12p12.1 (Figures 3D, S5D, and S5F). Downstream flow cytometry analysis revealed an increase in globosides Gb3, SSEA3, and Globo H as a consequence of ST8SIA1 deletion (Figures S5E and S5G). Because of the limited number of GSLs that can be studied using available antibodies by flow cytometry and to confirm the already observed dynamics of GSL expression, we utilized capillary gel electrophoresis coupled to laser-induced fluorescence detection (xCGE-LIF) to determine lipid glycosylation (Rossdam et al., 2019). In total, 19 GSLs were detected, representing all three GSL series with variations in abundance, comparing wild-type, ΔST8SIA1 (E-like), and ΔA4GALT (M -like) cells (Figure 3E). ΔA4GALT cells harboring M traits displayed enhanced sialylated (n)Lc4 and gangliosides accompanied by an expected loss of globosides investigated. In contrast, ΔST8SIA1 cells displayed elevated Gb3 and reduced GM2 as well as GM3 (Figure 3E), suggesting that ΔST8SIA1 cells underwent MET. This is in line with the observation that more GSLs carrying sialic acids are present at the cell surface of M-like cell lines, such as Tyk-nu and A2780, compared with the E-like BG1 cell line (Figure S5H). The characteristic EMT presence of globosides and gangliosides in OC cells harboring deletions in glycosyltransferase-encoding genes was in line with EMT marker expression; here, ΔST8SIA1 cells showed elevated E-cadherin, Claudin 1, Claudin 3, and EpCAM and reduced M markers N-Cadherin, β-catenin, and Slug, whereas ΔA4GALT cells revealed the opposite protein expression (Figures 3F and S5I).

Genetic deletion of ST8SIA1 induces MET in vitro and in vivo

Genomic deletion of ST8SIA1 enhanced expression of globosides and coincided with increased expression of E markers, suggesting that ΔST8SIA1 cells underwent MET (Figures 3 and S5). To characterize those cells, we performed various in vitro assays using wild-type, ΔST8SIA1, and ΔA4GALT cells representing intermediate, E-, and M-like phenotypes, respectively. Morphologically, induction of MET through ST8SIA1 knockout resulted in a significant 0.68-fold (2268 μm^2) decrease in average cell size (Figures 4A and S6B). We also observed morphological changes, where ΔST8SIA1 cells presented a cobblestone phenotype compared with the fibroblast-like morphology of ΔA4GALT (Figures S6A and S6B). MET has been postulated to be a critical event for tumor formation (Yao et al., 2011), addressed by in vitro and in vivo assays using anchorage-independent colony formation and in vivo tumor formation, respectively (Lau et al., 2021). We assessed the anchorage (in)dependent cell growth signature in our different cell lines and observed a significant increase in spheroids and colonies in ΔST8SIA1 cells, indicating that cells underwent MET (Figures 4B, 4C, and S6C). The E phenotype (ΔST8SIA1) retained elevated proliferation compared with M ΔA4GALT cells (Figures 4D–S6D). We also measured anchorage (in)dependent growth as well as cell proliferation in the presence of ΔST8SIA1 and control ΔAAVS1 in the M-like TOV112D and E-like SKOV3ip cell lines. Deletion of ST8SIA1 induced E characteristics in TOV112D cells, whereas SKOV3ip cells were
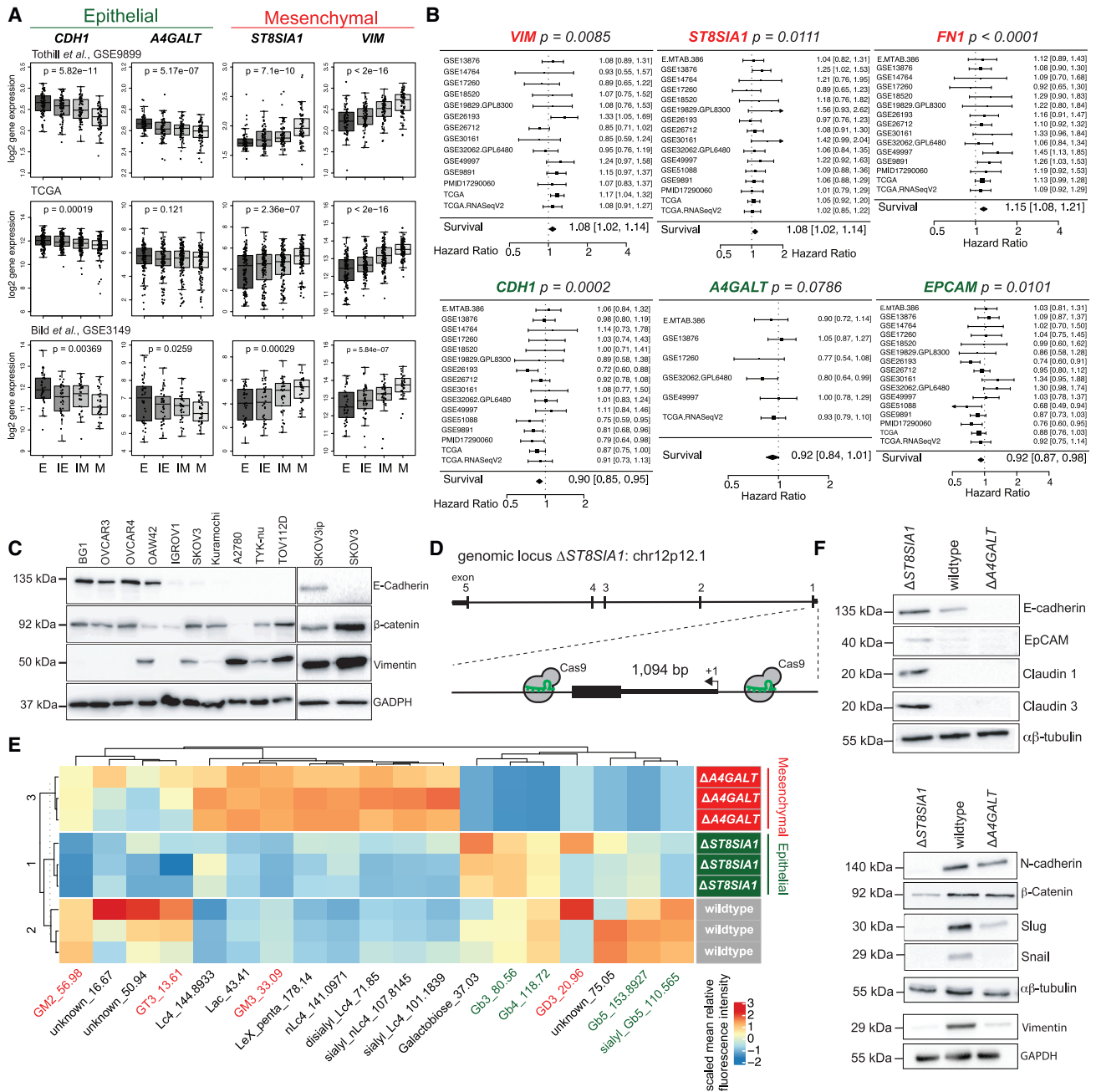
Figure 3. GSL glycosyltransferase encoding-genes follow EMT marker expression

(A) Boxplot with selected genes among four different EMT groups (epithelial [E], intermediate E [IE], intermediate mesenchymal [IM], and mesenchymal [M]); p value derived from ANOVA.

(B) Forest plots for selected EMT genes as univariate predictors of overall survival. Hazard ratio (HR) indicates the factor by which the overall risk of death increases with a 1 SD increase in expression; the p value for overall HR is indicated for each gene. Data were obtained from the curatedOvarianData database (Ganzfried et al., 2013).

(C) Western blot for EMT markers among OC cell lines.

(D) Strategy to generate a stable and site-specific *ST8SIA1* knockout (Δ*ST8SIA1)* in SKOV3 using CRISPR-Cas9.

(E) xCGE-LIF of enzymatically released and 8-aminopyrene-1,3,6-trisulfonic acid trisodium salt (APTS)-labeled glycans from GSLs. Quantification was performed based on relative signal fluorescence intensities.

(F) Western blot to confirm differential expression of E and M markers.

See also Figures S4 and S5.
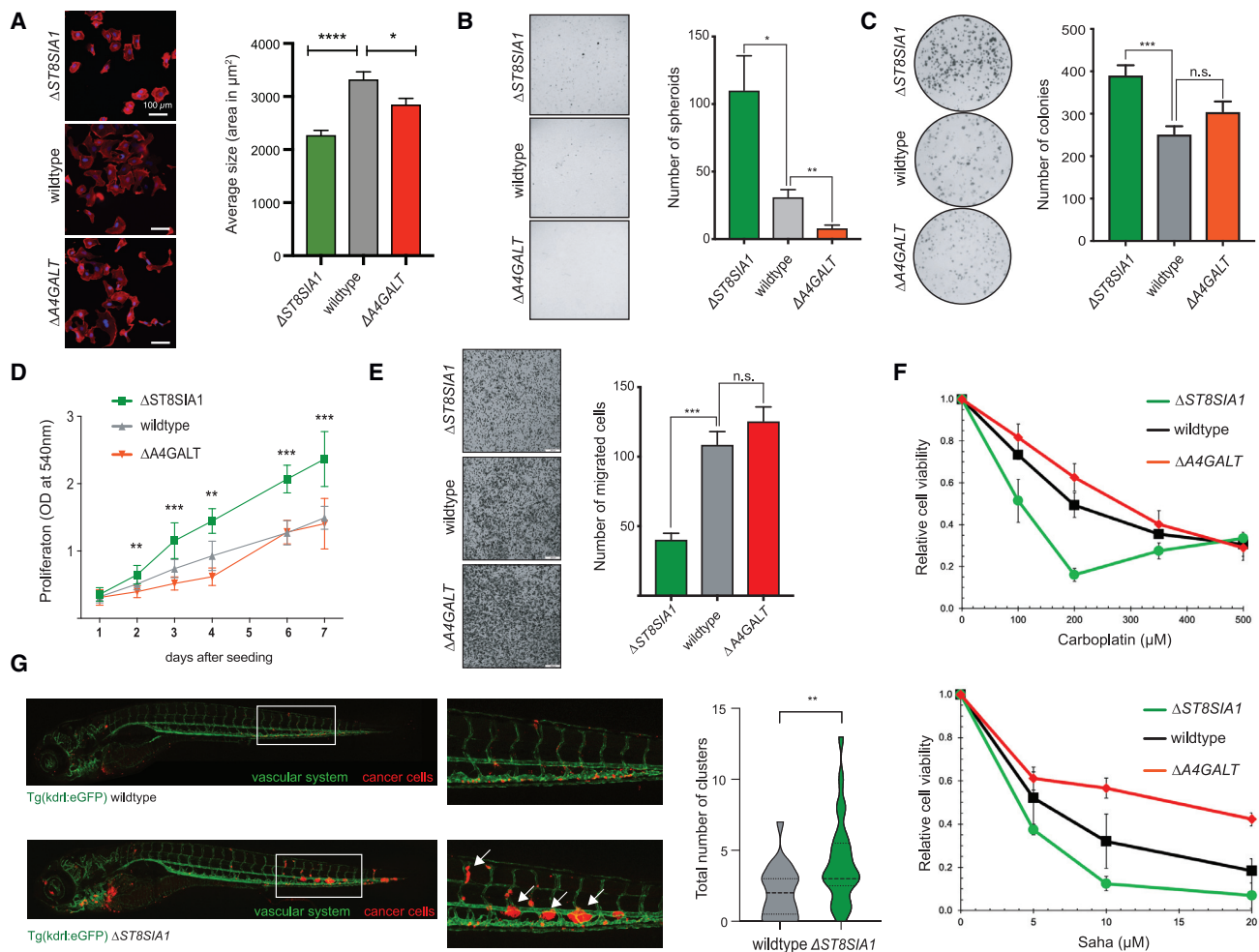
Figure 4. Deletion of *ST8SIA1* induces MET

(A) Phalloidin and DAPI staining for wild-type, Δ*ST8SIA1*, and Δ*A4GALT* cells with a corresponding bar chart representing the average cell size. Scale bar, 100 μm.

(B) Anchorage-independent growth with a corresponding bar chart quantifying the total number of spheroids (5,000 cells seeded and cultured for 15 days).

(C) Anchorage-dependent growth with increased numbers of colonies in Δ*ST8SIA1* cells compared with the wild-type and Δ*A4GALT*.

(D and E) Proliferation assay for wild-type (gray), Δ*A4GALT* (red), and Δ*ST8SIA1* (green) (D) and the corresponding migration assay (E). Scale bar, 200 μm.

(F) Concentration-dependent cell viability shown as a line chart (MTT cell viability) for the wild type, Δ*A4GALT*, and Δ*ST8SIA1*. There is increasing resistance in intermediate EMT cells deleted for Δ*A4GALT* and decreasing resistance in MET cells harboring Δ*ST8SIA1* deletion to carboplatin and SAHA. Data are presented as mean ± SD of at least three independent experiments performed in quadruplets.

(G) SKOV3 wild-type and Δ*ST8SIA1* (75–100 CM-DiI^{+}) cells were injected intravenously into zebrafish embryos. A quantification of total clusters compares the SKOV3 wild type and Δ*ST8SIA1* (n = 6 experiments, the violin plot summarizes 4–5 fish/group).

Student's t test; *p < 0.05, **p < 0.01, ***p < 0.001. Data are represented as mean ± SD. See also Figure S6.

marginally altered (Figures S6B and S6C). Previous studies have demonstrated that altered glycosylation enhances cancer cells' ability to disseminate (Hashiramoto et al., 2006). Thus, we investigated whether loss of *ST8SIA1* alters directed cell motility *in vitro*. As shown by the cell migration assay, there was a significant reduction in directed cell motility in Δ*ST8SIA1* cells compared with parental cells (Figure 4E). Acquired drug resistance has also been associated with EMT in various cancer types (Fischer et al., 2015; Zheng et al., 2015). Thus, we tested the cell viability of our knockout cells treated with various drugs and found that Δ*ST8SIA1* cells present enhanced sensitivity to carboplatin

and suberoylanilide hydroxamic acid (SAHA) compared with wild-type and Δ*A4GALT* cells (Figures 4F and S6E). The *in vitro* results suggest that depletion of sialylated gangliosides upon *ST8SIA1* deletion enhances cell proliferation while decreasing cell migration and viability. Because Δ*ST8SIA1* has marked effects on OC cells *in vitro*, we extended our research to zebrafish embryo tumor xenografts to validate our findings *in vivo*. Here, SKOV3 wild-type and Δ*ST8SIA1* cells were injected intravenously into the vasculature of transgenic *Tg(kdrl:EGFP)* zebrafish embryos. We detected significantly increased cluster formation at the tail for Δ*ST8SIA1* compared with wild-type cells, supporting
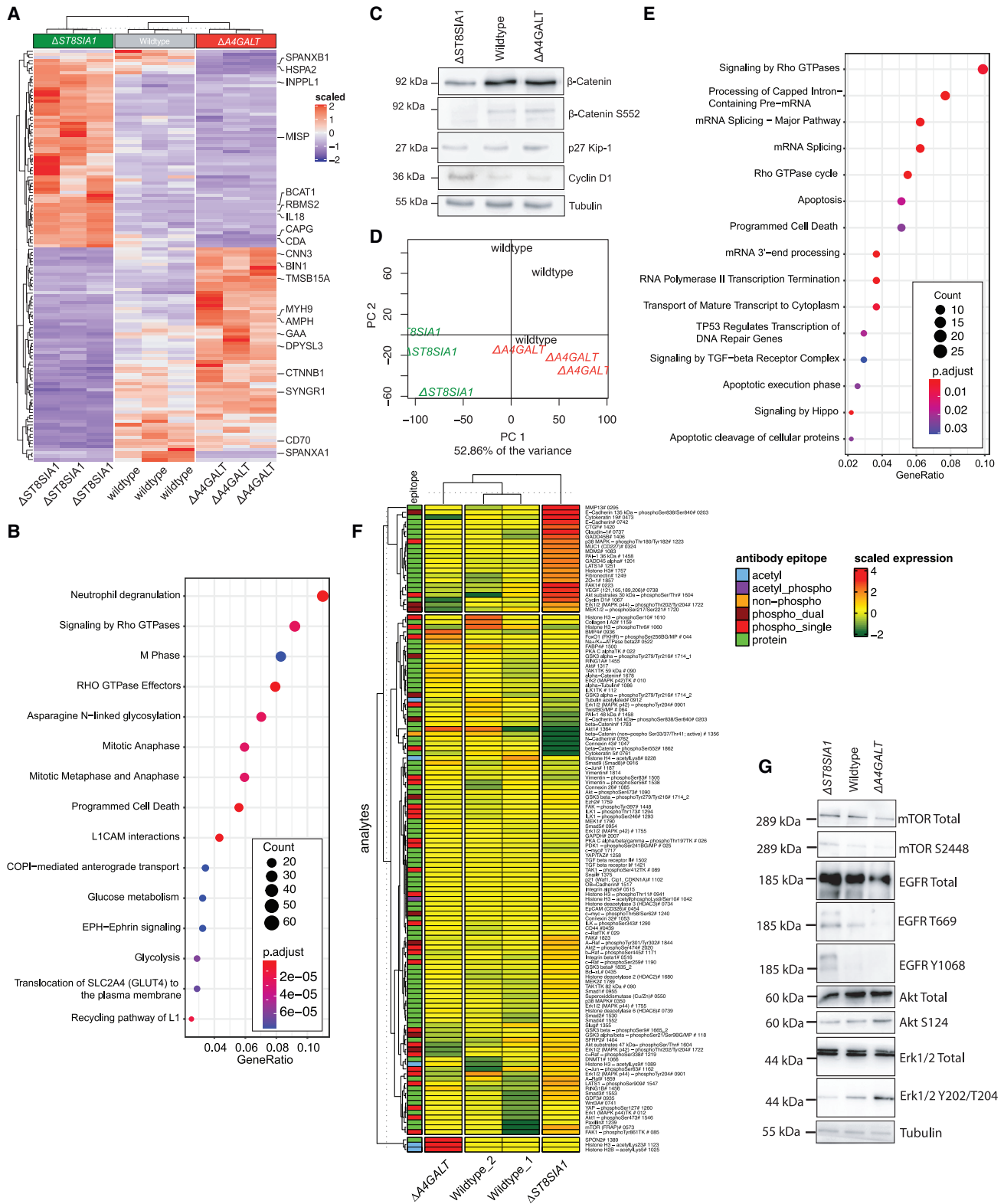
Figure 5. Phosphoproteomics analysis identifies GSL-dependent marker expression

(A) Unsupervised hierarchical clustering and heatmap for differentially expressed proteins (adjusted p < 0.05, n = 131).

(B) Gene Ontology (GO) enrichment analysis identified upregulated pathways (log$_2$ ≤ 1, adjusted p < 0.05) in ΔST8SIA1 cells.

(legend continued on next page)

the gained E features in those cells (Figure 4G). These results support that deletion of *ST8SIA1* in M-like OC cells results in MET accompanied by enhanced globoside expression and gain of E cell characteristics.

Phosphoproteomics in GSL-edited cells reveals distinct signaling pathways

The molecular mechanism underlying the alteration of GSL expression in OC cells that underwent MET remains uncertain. Therefore, we analyzed the proteome and the matched phosphoproteome in wild-type and different corresponding knockout cell lines (Figures 5, S7, and S8; Table S4). Unsupervised *k*-means hierarchical clustering revealed three independent clusters with distinct proteome signatures when comparing the wild-type, *ΔA4GALT*, and *ΔST8SIA1* cells (Figure 5A). Similarly, principal-component analysis (PCA), considering all quantified proteins, shows a separation of the different cell lines along the first principal component, which accounts for 45.2% of the variance in the data (Figure S7A). The wild-type, *ΔA4GALT*, and *ΔST8SIA1* proteomes were analyzed to investigate the intracellular regulation of various signaling pathways. Gene Ontology (GO) enrichment analysis indicated upregulation of signaling by Rho GTPase and cell cycle phases in the *ΔST8SIA1* cell line ($\log_2 \geq 1$, $p < 0.05$) (Figure 5B). These pathways are known to regulate cell cycle progression through cyclin D1 (Figure 5C; Croft and Olson, 2006; Villalonga and Ridley, 2006). In contrast, GO enrichment analysis of *ΔA4GALT* showed upregulation of the mitogen-activated protein kinase (MAPK) signaling pathway, which might play an important role in OC (Choi et al., 2003) ($\log_2 \geq 1$, $p < 0.05$) (Figure S7B). Analysis of matching phosphoproteomics data allowed us to identify a total of 11,342 phosphopeptides from a total of 2,985 proteins with a 0.01 false discovery rate (14,642 peptides spectrum matched [PSM]). PCA of all phosphoproteomics data separated along the first principal component with 52.9% of the variance (Figure 5D). In-depth pathway analysis using GO enrichment analysis revealed pathway enrichment for cell cycle and Rho GTPases ($\log_2 \geq 1$, $p < 0.05$) being upregulated in *ΔST8SIA1* (Figure 5E), which have been described to be essential for assembly and function of E cell-cell junctions (Braga et al., 1997; Hass et al., 1995). In our proteomics data, we also observed that the MAPK signaling pathway known to be involved in EMT (Gui et al., 2012) was also upregulated in *ΔA4GALT* (Figure S7B). We then investigated the 33 significantly altered phosphoproteins involved in the KEGG MAPK signaling pathway (hsa04010), comparing wild-type, *ΔST8SIA1*, and *ΔA4GALT* (Figure S7C). Here, we observed upregulation of AKT1, MAP3K2, and MAPK3 phosphorylation in *ΔA4GALT* cells, whereas EGFR and ERBB2 were upregulated in *ΔST8SIA1*. These data show that *ΔST8SIA1* is associated with a prolifera-

tive pathway, while *ΔA4GALT* correlates with the MAPK signaling pathway. A previous study demonstrated that MET is induced through upregulation of cyclic AMP (cAMP) and cAMP-dependent protein kinase A (PKA or *PRKACA*) (Pattabiraman et al., 2016). It has also been shown that PKA activation inhibits Erk1/2 (Mischak et al., 1996). The KEGG pathview package allowed us to visualize phosphoproteins in the cAMP pathway signaling for *ΔST8SIA1* using wild-type cells as reference. We observed that PKA phosphorylation was activated, accompanied by downregulation of Erk1/2 in *ΔST8SIA1* (Figure S8A). In line with this, multiple proteins involved in cAMP signaling with altered phosphorylation were identified, highlighting a significant decrease of PDE1C^{S469} in *ΔST8SIA1* (Figure S7D), a phosphorylation site that has been reported to enhance cAMP activation (Kogiso et al., 2017). We also observed significant downregulation of phosphorylation of Erk^{T185} (MAPK1) as well as the proto-oncogene c-JUN^{S63} in *ΔST8SIA1* cells (Figure S7D). Erk1/2 inhibition has been reported to downregulate c-Jun phosphorylation in cervical cancer (Bai et al., 2015) and has been functionally linked to altering cell motility in OC (Hein et al., 2009). We confirmed the sites reported here to be involved in EMT upon deletion of key glycosyltransferases by integrating phosphoproteomics, DigiWest, and western blot, identifying consistently altered phosphorylation sites (Figures 5G and S8C; Table S4).

The abundance of sialic acid-bearing GSLs coincides with calcium-mediated signaling regulation

Our phosphoproteomics analysis revealed pathways associated with synaptic and Ca^{2+}-mediated signaling in M-like *ΔA4GALT* cells (Figure S9A). A previous study demonstrated that Ca^{2+} could bind to sialic acids (Jaques et al., 1977). Thus, we hypothesized that gangliosides, as a major series of sialic acid-bearing GSLs on cancer cells, might be actively involved in regulation of Ca^{2+}-mediated signaling pathways. We initially assessed publicly available single-cell RNA sequencing (RNA-seq) data on various cancer cell lines to analyze the Ca^{2+} dependency between E and M cancer cells (Figure 6A). These analyses revealed that M-like cancer cells are more Ca^{2+} dependent compared with E-like cells (Figure 6A). Subsequently, we investigated the KEGG hsa04020:calcium signaling pathway in our cell line panel and found differentially phosphorylated peptides (n = 31 proteins), with CAMK2D, CAMK2B, and CAMK4 showing elevated phosphopeptides in *ΔA4GALT* compared with *ΔST8SIA1* (Figures 6B and S9B), shown previously to enhance EMT-associated cell motility through Ca^{2+} signaling (Chi et al., 2016). To assess the involvement of Ca^{2+} in our gene-edited cell lines, we deprived culture medium of Ca^{2+} for 24 h, reintroduced Ca^{2+}, and measured phosphorylation sites at different time points (Figure 6C). A reduction of

---

(C) Western blot with Cyclin D1, p27 Kip-1, β-catenin, and β-catenin^{S552} expression in the wildtype, *ΔST8SIA1*, and *ΔA4GALT*.

(D) PCA of the phosphoproteome comparing parental and EMT-driven glyco-gene knockout cells (n = 3 independent experiments) with a $\log_2$-fold change using the singular value decomposition (SVD) method to perform the PCA.

(E) GO enrichment analysis identified upregulated pathways in *ΔST8SIA1* cells based on phosphoproteomics.

(F) Heatmap representing the different antibodies tested from DigiWest for SKOV3ip, SKOV3, *ΔST8SIA1*, and *ΔA4GALT*.

(G) Western blot showing major changes of phosphoproteins in the PI3K/AKT and MAPK signaling pathways.

See also Figures S7 and S8 and Table S4.
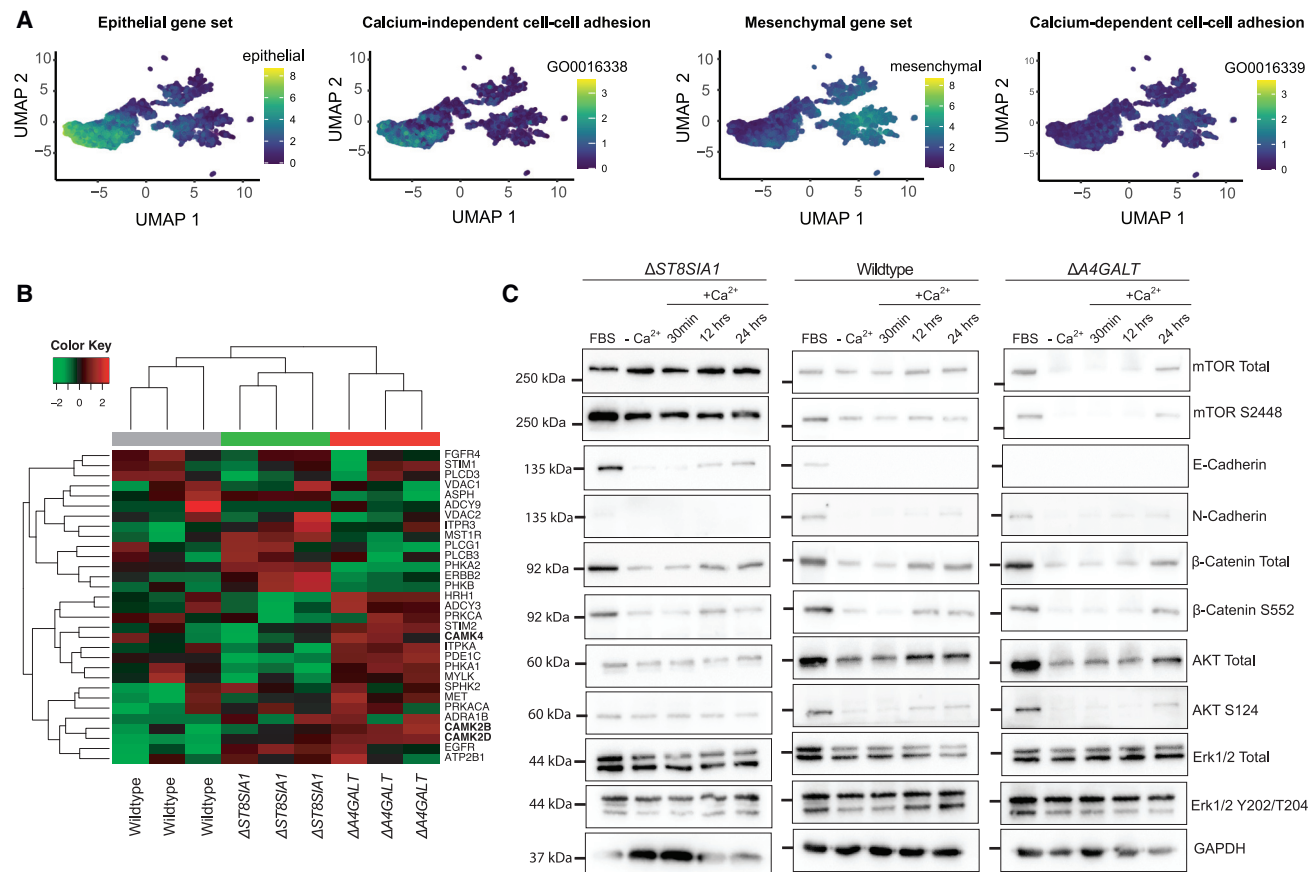
Figure 6. Extracellular calcium regulates specific phosphorylation sites through sialic acid-terminated GSLs

(A) UMAP based on single-cell RNA-seq (scRNA-seq) analysis of cell lines, showing clustering of E and M states.

(B) Heatmap of the KEGG hsa04020: calcium signaling pathway. Data were analyzed based on three biological replicates of the wild type, ΔST8SIA1, and ΔA4GALT.

(C) Western blot showing major changes of phosphorylation in the MAPK and PI3K/AKT pathways upon reduction of calcium for 24 h in wild-type and ΔA4GALT cells.

See also Figure S9.

extracellular Ca^{2+} in ΔST8SIA1 cells marginally altered phosphorylation of the MAPK ($Erk^{Y202/T204}$) pathways but reduced phosphorylation of $mTOR^{S2248}$ or AKT^{S124}. Ca^{2+} deprivation in wild-type cells did not affect $mTOR^{S2448}$ phosphorylation but reduced Akt^{S124} and $Erk^{T202/Y204}$ phosphorylation. This effect was recovered after reintroducing Ca^{2+} for 12 h. Regarding ΔA4GALT cells, reducing extracellular Ca^{2+} affected Akt^{S124}, $Erk^{T202/Y204}$, and $mTOR^{S2448}$ and reached basal levels after 24 h in the presence of Ca^{2+}. These data demonstrate that cells enriched in sialylated GSLs might be more sensitive to extracellular Ca^{2+} deprivation, as shown by prolonged time to recover the phosphatidylinositol 3-kinase (PI3K)/AKT signaling pathway. We also investigated the effect of intracellular Ca^{2+} regulation in our gene-edited cells using the cell-permeable Ca^{2+} chelator. Addition of BAPTA-AM increased E marker expression in ΔST8SIA1 and wild-type cells only (Figure S9C). Finally, to confirm that ganglioside-depleted cells are more sensitive to intracellular Ca^{2+} stability, we measured cell proliferation using BAPTA-AM treatment and observed an overall

reduction of proliferation for all cell lines but more profound for ΔST8SIA1 cells (Figure S9D).

DISCUSSION

We demonstrate that globosides are enriched in cancer cells and in the tumor compartment of tissue from affected individuals that is commonly characterized by E-cadherin. We show that M marker expression correlates with elevated gangliosides and that, consequently, cancer cells harboring genomic deletion of the glycosyltransferase-encoding gene ST8SIA1 acquire E-like features accompanied by reduction of gangliosides and enrichment of globosides. Finally, GSL-mediated transition of intermediate EMT cancer cells into E (ΔST8SIA1) or M (ΔA4GALT) is promoted by distinct signaling pathways with a ganglioside calcium dependency in M-like cells. Besides in vitro and in vivo EMT-defining characteristics, bimodal (phospho)proteomics also points toward differential intracellular Ca^{2+} regulation depending on GSL composition coinciding with M features.

Our data establish that tumor-specific E-cadherin expression is maintained but significantly reduced in the metastatic lesions (dominated by omentum and peritoneal implants) compared with the respective primary tubo-ovarian tumor at the time of diagnosis. In contrast, E-cadherin expression remained stable throughout the course of the disease, even at the time of recurrence, suggesting that most OCs maintain their E characteristics. This finding supports the literature (Fujimoto et al., 1997; Fujioka et al., 2001) suggesting that E-cadherin is important in formation of metastatic lesions and is maintained during tumor progression. We also demonstrated that OC tissue showed elevated globosides, whereas ascites were slightly enriched in gangliosides. These data were confirmed by Santin et al. (2004) reporting an increase in gangliosides in ascites fluid from OC and by Liang et al. (2013) showing a reduction in Fuc-(n)Lc4Cer and Gb3Cer accompanied by elevated gangliosides in CD24^{low}CD44^{high} breast cancer cells. In line with this, our findings extend the current literature by another cancer type with a similar genomic landscape (Cancer Genome Atlas Network, 2012). To gain better insight into the distribution of GSLs in snap-frozen OC samples, we applied spatial glycosphingolipidomics and found that the tumor compartment was enriched for globosides reported previously in E tumor models (Jacob et al., 2018; Kovbasnjuk et al., 2005; Park et al., 2012). On the other hand, MALDI-MSI demonstrated that gangliosides are preferentially elevated in the stroma region characterized by M marker expression (Karnoub et al., 2007). This observation is supported by reports of gangliosides being elevated in tissues or cell types characterized by M-like signatures (Dobrenkov et al., 2016; Martinez et al., 2007; Xu et al., 2009). We also functionally demonstrate that endogenous truncation of the E-cadherin cytoplasmic tail in E OC cells results in partial EMT accompanied by loss of globosides, supporting the hypothesis that GSL composition may define the plasticity of cancer cells and indicating that these biomolecules are actively involved in EMT. Functional E-cadherin is considered the hallmark of EMT (Gheldof and Berx, 2013), and studies have evaluated its expression in OC tissue samples and cell lines. E-cadherin has been implicated as a predictor of improved response to first-line chemotherapy in high-grade serous OC (Miše et al., 2015), which is in line with the suppression of invasiveness character of E-cadherin reported in ovarian surface E cells (Shi et al., 2020). Also, mutations in the genomic locus of *CDH1* have been described with high prevalence together with *TP53* and *ARID1A* in gastric cancer; here, enrichment of *CDH1* aberrations in undifferentiated mucinous gastric carcinoma has been reported (Rokutan et al., 2016).

The analysis of transcriptomics data revealed various sialyltransferase-encoding genes that are enriched in cell lines with elevated M markers. We did not find strong evidence of an association of OC subtypes and EMT, neither in the cell lines investigated nor for E-cadherin expression on tissue microarrays, with the exception of metastatic sites only. The literature also suggests that EMT is a cell-type-dependent phenomenon and does not dictate oncogenesis (Bhagirath et al., 2016). Therefore, the effect of somatic mutations incurred during tumor formation and metastasis on EMT remains to be elucidated (Lambert et al., 2017). We selected SKOV3 because it is a frequently applied OC

cell line in the literature regarding EMT. In addition, SKOV3ip, TOV112D, and BG1 were chosen because they represent various EMT states and are more susceptible to proceeding through a spectrum of intermediate states compared with full E or M cancer cells. Among the MET-associated glycosyltransferases-encoding genes, transcriptomics consistently identified *ST8SIA1* as the most robust candidate from the GSL pathway-annotated genes, following mesenchymal marker expression and predicting poor prognosis. Thus, we hypothesized that deletion of *ΔST8SIA1* may induce MET; we have recently demonstrated that cells harboring *ΔA4GALT* undergo EMT through DNA hypermethylation or elevated M transcription factor binding at the *CDH1* promoter region (Jacob et al., 2018). *ST8SIA1* encodes for the glycosyltransferase GD3 synthase (GD3S) and has been suggested to be important for initiation and maintenance of EMT using RNAi in MDA-MB-231. Battula et al. (2012) reported increased GD2 and GD3S expression upon pharmacological induction of EMT. Data for gliomas defined as M tumors (Tan et al., 2014) suggest that ST8SIA1 enhances glioma progression accompanied by reduced Akt^{S473} phosphorylation (Ohkawa et al., 2021). Our study provides evidence showing that genomic deletion of *ST8SIA1* accompanied by elevated E markers coincided with reduction of gangliosides, enrichment of globosides, and *in vitro* characteristics usually associated with MET (Pei et al., 2019). The controversial existence of MET at metastatic sites has been postulated to be part of the process of metastatic tumor formation (Chaffer et al., 2007). Our data on E-like *ΔST8SIA1* cells revealed reduced cell migration and enhanced drug sensitivity compared with wild-type and *ΔA4GALT* cells and, thus, correlate with work in breast cancer (Sarkar et al., 2015). *ΔST8SIA1* cells acquired traits associated with E characteristics, which led to an increase in cell proliferation and formation of colonies and spheroids. Existing data associate loss of GD3 and silencing or pharmacological inhibition of ST8SIA1 with altered cell morphology causing increased clustering of cells into E-like islands. Establishment of cell-cell contacts and reduced fibroblastic morphology accompanied by decreased M marker expression of N-cadherin, fibronectin, and vimentin have been reported in the absence of ST8SIA1 in breast cancer (Sarkar et al., 2015). Overexpression of ST8SIA1 increases cell migration (Cazet et al., 2009), suggesting that enrichment of gangliosides is associated with features of EMT. Our observations in *ΔA4GALT* or *ΔST8SIA1* support the hypothesis of active involvement of GSLs in reversible EMT.

To mechanistically dissect the role in EMT, our phosphoproteomics approach in wild-type (intermediate EMT) and gene-edited cells revealed involvement of EMT- and MET-associated signaling pathways. On one hand, we found the Rho GTPase family being activated during MET in *ΔST8SIA1*. This finding correlates with work demonstrating that the Rho GTPase Rnd1 inhibits the MAPK pathway through reduction of Erk$^{T202/Y204}$ phosphorylation, inducing EMT suppression (Okada et al., 2015; Qin et al., 2018). The *ST8SIA1* deletion decreased activation of Erk, Akt, and β-catenin in OC cells, supporting studies in prostate and breast cancer (Nguyen et al., 2018; Wan et al., 2021; Xing et al., 2021). HER2/EGFR signaling was activated in *ΔST8SIA1* compared with *ΔA4GALT*. Previous work demonstrated that activation of HER2/EGFR switches

transforming growth factor β (TGF-β) from inhibiting cell proliferation to promoting cell migration, and attenuated TGF-β induces EMT migration in breast cancer (Huang et al., 2018).

Exogenously induced EMT produces a transient increase in intracellular Ca^{2+} in breast cancer cells (Davis et al., 2014). Our GO analysis of $\Delta A4GALT$ also showed enrichment of calcium-dependent pathways. Single-cell RNA-seq analysis associated M markers with calcium-associated signaling pathways. In line with the $\Delta A4GALT$ cells reported here, a recent study demonstrated that genetic loss of the globoside enzyme *B3GALT5* may facilitate primed-to-naive conversion in stem cells by raising intracellular Ca^{2+} (Lin et al., 2020). Another study reported that sialic acids are strongly and preferentially complexed with Ca^{2+} (Jaques et al., 1977). Intrigued by these observations and additional studies reporting calcium dependency during EMT in ovarian and breast cancer with activated MAPK signaling (Chao et al., 1992; Davis et al., 2014; Liu et al., 2019), we postulate that sialic acids on GSLs (mostly gangliosides) may be involved in uptake and regulation of intracellular Ca^{2+} in cancer cells with M features, a process that is hampered upon genetic deletion of *ST8SIA*.

Limitations of the study

In this study, we used various experimental methods to provide evidence of the active involvement of GSLs in reversible EMT. Although the cellular-state dynamics result in phenotypic heterogeneity in several OC cell lines as reported in this study, our results may not directly translate to the pathology of the most common subtype of high-grade serous OC, considering the reported mutational landscape and potential associations with EMT. MALDI-MSI was performed in tumor tissue samples only, and the data reported are therefore not necessarily reflective of GSLs from "normal" cells (e.g., fallopian tube or ovarian surface epithelium). Association of the *m/z* value with a specific GSL relies on mass accuracy and previously reported literature. We also overlooked the potential involvement of the ceramide composition of GSLs reported here. Finally, the mechanism of how GSLs could regulate the flux of calcium through the cell membrane remains to be elucidated.

STAR★METHODS

Detailed methods are provided in the online version of this paper and include the following:

- KEY RESOURCES TABLE
- RESOURCE AVAILABILITY
  - Lead contact
  - Materials availability
  - Data and code availability
- EXPERIMENTAL MODEL AND SUBJECT DETAILS
  - Patient-derived tissue
  - Slow-frozen tissue samples for GSL expression determined by flow cytometry
  - Snap-frozen tissue samples for MALDI imaging
  - Cell lines
- METHOD DETAILS
  - Immunohistochemistry
- Image analysis
  - Access to publicly available bulk transcriptomic data and analysis
  - Analysis of single-cell RNAseq data
  - MALDI-mass spectrometer imaging (MSI)
  - Cell culture
  - Molecular cloning
  - Generation of homozygously deleted ΔST8SIA1 cell lines
  - Lentiviral transduction for generating *ST8SIA1* mutant cells
  - Genotyping PCR
  - Generation of E-cadherin knock-in cell lines
  - Patient-derived OC sample dissociation
  - Flow cytometry analysis
  - *In vivo* xenografts using zebrafish embryos
  - Multiplexed capillary gel electrophoresis coupled to laser-induced fluorescence detection (xCGE-LIF)
  - DigiWest
  - Mass spectrometry based phosphoproteomics analysis
  - Reactome pathway enrichment analysis
  - Proliferation assay
  - Anchorage independent growth
  - Anchorage dependent growth
  - Migration assay
  - Immunofluorescence staining and imaging
  - Immunoblotting
- QUANTIFICATION AND STATISTICAL ANALYSIS

AUTHOR CONTRIBUTIONS

Conceptualization, C.C., V.H.-S., and F.J.; methodology, C.C., A.E.-D., S.P.C., F.C.L., N.R., S.A., A.S., D.C., A.F., and F.J.; investigation, C.C., A.E.-D., S.P.C., Y.-L.H., C.-Y.L., F.C.L., R.C., N.R., M.K., S.A., A.S., D.C., A.F., and F.J.; data curation, C.C., A.E.-D., C.R., F.R., S.P.C., M.N.L., D.C., and F.J.; writing—original draft, C.C., A.E.-D., R.C., and F.J.; writing – review & editing, all authors; visualization, C.C., A.E.-D., C.R., F.R., S.P.C., F.C.L., D.C., A.F., and F.J.; supervision, A.E.-D., A.S., T.V., M.v.I., C.-Y.L., M.T., F.F.R.B., V.H.-S., and F.J.; project administration, F.J.; funding acquisition, A.E.-D., M.v.I., M.T., F.F.R.B., V.H.-S., and F.J.

CellPress
OPEN ACCESS

REFERENCES

Alam, S., Anugraham, M., Huang, Y.-L., Kohler, R.S., Hettich, T., Winkelbach, K., Grether, Y., López, M.N., Khasbiullina, N., Bovin, N.V., et al. (2017). Altered (neo-) lacto series glycolipid biosynthesis impairs α2-6 sialylation on N-glycoproteins in ovarian cancer cells. Sci. Rep. 7, 45367. https://doi.org/10.1038/srep45367.

Angel, P.M., Spraggins, J.M., Baldwin, H.S., and Caprioli, R. (2012). Enhanced sensitivity for high spatial resolution lipid analysis by negative ion mode matrix assisted laser desorption ionization imaging mass spectrometry. Anal. Chem. 84, 1557–1564. https://doi.org/10.1021/ac202383m.

Auersperg, N., Pan, J., Grove, B.D., Peterson, T., Fisher, J., Maines-Bandiera, S., Somasiri, A., and Roskelley, C.D. (1999). E-cadherin induces mesenchymal-to-epithelial transition in human ovarian surface epithelium. Proc. Natl. Acad. Sci. USA 96, 6249–6254. https://doi.org/10.1073/pnas.96.11.6249.

Bai, L., Mao, R., Wang, J., Ding, L., Jiang, S., Gao, C., Kang, H., Chen, X., Sun, X., and Xu, J. (2015). ERK1/2 promoted proliferation and inhibited apoptosis of human cervical cancer cells and regulated the expression of c-Fos and c-Jun proteins. Med. Oncol. 32, 57. https://doi.org/10.1007/s12032-015-0490-5.

Barretina, J., Caponigro, G., Stransky, N., Venkatesan, K., Margolin, A.A., Kim, S., Wilson, C.J., Lehár, J., Kryukov, G.V., Sonkin, D., et al. (2012). The Cancer Cell Line Encyclopedia enables predictive modelling of anticancer drug sensitivity. Nature 483, 603–607. https://doi.org/10.1038/nature11003.

Battula, V.L., Shi, Y., Evans, K.W., Wang, R.-Y., Spaeth, E.L., Jacamo, R.O., Guerra, R., Sahin, A.A., Marini, F.C., Hortobagyi, G., et al. (2012). Ganglioside GD2 identifies breast cancer stem cells and promotes tumorigenesis. J. Clin. Invest. 122, 2066–2078. https://doi.org/10.1172/JCI59735.

Bhagirath, D., Zhao, X., Mirza, S., West, W.W., Band, H., and Band, V. (2016). Mutant PIK3CA induces EMT in a cell type specific manner. PLoS One 11, e0167064. https://doi.org/10.1371/journal.pone.0167064.

Bien, T., Perl, M., Machmüller, A.C., Nitsche, U., Conrad, A., Johannes, L., Müthing, J., Soltwisch, J., Janssen, K.-P., and Dreisewerd, K. (2020). MALDI-2 mass spectrometry and immunohistochemistry imaging of Gb3Cer, Gb4Cer, and further glycosphingolipids in human colorectal cancer tissue. Anal. Chem. 92, 7096–7105. https://doi.org/10.1021/acs.analchem.0c00480.

Braga, V.M., Machesky, L.M., Hall, A., and Hotchin, N.A. (1997). The small GTPases Rho and Rac are required for the establishment of cadherin-dependent cell-cell contacts. J. Cell Biol. 137, 1421–1431. https://doi.org/10.1083/jcb.137.6.1421.

Cancer Genome Atlas Network (2012). Comprehensive molecular portraits of human breast tumours. Nature 490, 61–70. https://doi.org/10.1038/nature11412.

Cazet, A., Groux-Degroote, S., Teylaert, B., Kwon, K.-M., Lehoux, S., Slomianny, C., Kim, C.-H., Le Bourhis, X., and Delannoy, P. (2009). GD3 synthase overexpression enhances proliferation and migration of MDA-MB-231 breast cancer cells. Biol. Chem. 390, 601–609. https://doi.org/10.1515/BC.2009.054.

Chaffer, C.L., Thompson, E.W., and Williams, E.D. (2007). Mesenchymal to epithelial transition in development and disease. Cells Tissues Organs (Print) 185, 7–19. https://doi.org/10.1159/000101298.

Chang, F., Li, R., Noon, K., Gage, D., and Ladisch, S. (1997). Human medulloblastoma gangliosides. Glycobiology 7, 523–530. https://doi.org/10.1093/glycob/7.4.523.

Chao, T.S., Byron, K.L., Lee, K.M., Villereal, M., and Rosner, M.R. (1992). Activation of MAP kinases by calcium-dependent and calcium-independent pathways. Stimulation by thapsigargin and epidermal growth factor. J. Biol. Chem. 267, 19876–19883.

Chen, H.-N., Yuan, K., Xie, N., Wang, K., Huang, Z., Chen, Y., Dou, Q., Wu, M., Nice, E.C., Zhou, Z.-G., and Huang, C. (2016). PDLIM1 stabilizes the E-cadherin/β-catenin complex to prevent epithelial-mesenchymal transition and metastatic potential of colorectal cancer cells. Cancer Res. 76, 1122–1134. https://doi.org/10.1158/0008-5472.CAN-15-1962.

Chi, M., Evans, H., Gilchrist, J., Mayhew, J., Hoffman, A., Pearsall, E.A., Jankowski, H., Brzozowski, J.S., and Skelding, K.A. (2016). Phosphorylation of calcium/calmodulin-stimulated protein kinase II at T286 enhances invasion and migration of human breast cancer cells. Sci. Rep. 6, 33132. https://doi.org/10.1038/srep33132.

Choi, K.-C., Auersperg, N., and Leung, P.C.K. (2003). Mitogen-activated protein kinases in normal and (pre)neoplastic ovarian surface epithelium. Reprod. Biol. Endocrinol. 1, 71. https://doi.org/10.1186/1477-7827-1-71.

Colsch, B., and Woods, A.S. (2010). Localization and imaging of sialylated glycosphingolipids in brain tissue sections by MALDI mass spectrometry. Glycobiology 20, 661–667. https://doi.org/10.1093/glycob/cwq031.

Croft, D.R., and Olson, M.F. (2006). The Rho GTPase effector ROCK regulates cyclin A, cyclin D1, and p27Kip1 levels by distinct mechanisms. Mol. Cell Biol. 26, 4612–4627. https://doi.org/10.1128/MCB.02061-05.

Cumin, C., Huang, Y.-L., Everest-Dass, A., and Jacob, F. (2021). Deciphering the importance of glycosphingolipids on cellular and molecular mechanisms associated with epithelial-to-mesenchymal transition in cancer. Biomolecules 11, 62. https://doi.org/10.3390/biom11010062.

Davis, F.M., Azimi, I., Faville, R.A., Peters, A.A., Jalink, K., Putney, J.W., Goodhill, G.J., Thompson, E.W., Roberts-Thomson, S.J., and Monteith, G.R. (2014). Induction of epithelial-mesenchymal transition (EMT) in breast cancer cells is calcium signal dependent. Oncogene 33, 2307–2316. https://doi.org/10.1038/onc.2013.187.

Dobrenkov, K., Ostrovnaya, I., Gu, J., Cheung, I.Y., and Cheung, N.-K.V. (2016). Oncotargets GD2 and GD3 are highly expressed in sarcomas of children, adolescents, and young adults. Pediatr. Blood Cancer 63, 1780–1785. https://doi.org/10.1002/pbc.26097.

Domcke, S., Sinha, R., Levine, D.A., Sander, C., and Schultz, N. (2013). Evaluating cell lines as tumour models by comparison of genomic profiles. Nat. Commun. 4, 2126. https://doi.org/10.1038/ncomms3126.

Dunfield, L.D., Dwyer, E.J.C., and Nachtigal, M.W. (2002). TGF beta-induced Smad signaling remains intact in primary human ovarian cancer cells. Endocrinology 143, 1174–1181. https://doi.org/10.1210/endo.143.4.8733.

Ermini, L., Morganti, E., Post, A., Yeganeh, B., Caniggia, I., Leadley, M., Faria, C.C., Rutka, J.T., and Post, M. (2017). Imaging mass spectrometry identifies prognostic ganglioside species in rodent intracranial transplants of glioma and medulloblastoma. PLoS One 12, e0176254. https://doi.org/10.1371/journal.pone.0176254.

Federico, S.M., McCarville, M.B., Shulkin, B.L., Sondel, P.M., Hank, J.A., Hutson, P., Meagher, M., Shafer, A., Ng, C.Y., Leung, W., et al. (2017). A pilot trial of humanized anti-GD2 monoclonal antibody (hu14.18K322A) with chemotherapy and natural killer cells in children with recurrent/refractory neuroblastoma. Clin. Cancer Res. 23, 6441–6449. https://doi.org/10.1158/1078-0432.CCR-17-0379.

Fischer, K.R., Durrans, A., Lee, S., Sheng, J., Li, F., Wong, S.T.C., Choi, H., El Rayes, T., Ryu, S., Troeger, J., et al. (2015). Epithelial-to-mesenchymal transition is not required for lung metastasis but contributes to chemoresistance. Nature 527, 472–476. https://doi.org/10.1038/nature15748.

Fujimoto, J., Ichigo, S., Hirose, R., Sakaguchi, H., and Tamaya, T. (1997). Suppression of E-cadherin and alpha- and beta-catenin mRNA expression in the metastatic lesions of gynecological cancers. Eur. J. Gynaecol. Oncol. 18, 484–487.

Fujioka, T., Takebayashi, Y., Kihana, T., Kusanagi, Y., Hamada, K., Ochi, H., Uchida, T., Fukumoto, M., and Ito, M. (2001). Expression of E-cadherin and

beta-catenin in primary and peritoneal metastatic ovarian carcinoma. Oncol. Rep. *8*, 249–255.

Ganzfried, B.F., Riester, M., Haibe-Kains, B., Risch, T., Tyekucheva, S., Jazic, I., Wang, X.V., Ahmadifar, M., Birrer, M.J., Parmigiani, G., et al. (2013). curate-dOvarianData: clinically annotated data for the ovarian cancer transcriptome. Database *2013*, bat013. https://doi.org/10.1093/database/bat013.

George, J.T., Jolly, M.K., Xu, S., Somarelli, J.A., and Levine, H. (2017). Survival outcomes in cancer patients predicted by a partial EMT gene expression scoring metric. Cancer Res. *77*, 6415–6428. https://doi.org/10.1158/0008-5472.CAN-16-3521.

Gheldof, A., and Berx, G. (2013). Cadherins and epithelial-to-mesenchymal transition. Prog. Mol. Biol. Transl. Sci. *116*, 317–336. https://doi.org/10.1016/B978-0-12-394311-8.00014-5.

Gooding, A.J., and Schiemann, W.P. (2020). Epithelial-mesenchymal transition programs and cancer stem cell phenotypes: mediators of breast cancer therapy resistance. Mol. Cancer Res. *18*, 1257–1270. https://doi.org/10.1158/1541-7786.MCR-20-0067.

Gui, T., Sun, Y., Shimokado, A., and Muragaki, Y. (2012). The roles of mitogen-activated protein kinase pathways in TGF-β-induced epithelial-mesenchymal transition. J. Signal Transduct. *2012*, 289243. https://doi.org/10.1155/2012/289243.

Hashiramoto, A., Mizukami, H., and Yamashita, T. (2006). Ganglioside GM3 promotes cell migration by regulating MAPK and c-Fos/AP-1. Oncogene *25*, 3948–3955. https://doi.org/10.1038/sj.onc.1209416.

Hass, U., Jakobsen, B.M., and Lund, S.P. (1995). Developmental toxicity of inhaled N-methylpyrrolidone in the rat. Pharmacol. Toxicol. *76*, 406–409. https://doi.org/10.1111/j.1600-0773.1995.tb00170.x.

He, X., Tan, C., Wang, F., Wang, Y., Zhou, R., Cui, D., You, W., Zhao, H., Ren, J., and Feng, B. (2016). Knock-in of large reporter genes in human cells via CRISPR/Cas9-induced homology-dependent and independent DNA repair. Nucleic Acids Res. *44*, e85. https://doi.org/10.1093/nar/gkw064.

Hein, S., Mahner, S., Kanowski, C., Löning, T., Jänicke, F., and Milde-Langosch, K. (2009). Expression of Jun and Fos proteins in ovarian tumors of different malignant potential and in ovarian cancer cell lines. Oncol. Rep. *22*, 177–183. https://doi.org/10.3892/or_00000422.

Hirsch, F.R., Varella-Garcia, M., Bunn, P.A., Di Maria, M.V., Veve, R., Bremmes, R.M., Barón, A.E., Zeng, C., and Franklin, W.A. (2003). Epidermal growth factor receptor in non-small-cell lung carcinomas: correlation between gene copy number and protein expression and impact on prognosis. J. Clin. Oncol. *21*, 3798–3807. https://doi.org/10.1200/JCO.2003.11.069.

Huang, F., Shi, Q., Li, Y., Xu, L., Xu, C., Chen, F., Wang, H., Liao, H., Chang, Z., Liu, F., et al. (2018). HER2/EGFR-AKT signaling switches TGFβ from inhibiting cell proliferation to promoting cell migration in breast cancer. Cancer Res. *78*, 6073–6085. https://doi.org/10.1158/0008-5472.CAN-18-0136.

Huang, R.Y.J., Wong, M.K., Tan, T.Z., Kuay, K.T., Ng, A.H.C., Chung, V.Y., Chu, Y.S., Matsumura, N., Lai, H.C., Lee, Y.F., et al. (2013). An EMT spectrum defines an anoikis-resistant and spheroidogenic intermediate mesenchymal state that is sensitive to e-cadherin restoration by a src-kinase inhibitor, saracatinib (AZD0530). Cell Death Dis. *4*, e915. https://doi.org/10.1038/cddis.2013.442.

Huang, Y.-L., Liang, C.-Y., Ritz, D., Coelho, R., Septiadi, D., Estermann, M., Cumin, C., Rimmer, N., Schötzau, A., Núñez López, M., et al. (2020). Collagen-rich omentum is a premetastatic niche for integrin α2-mediated peritoneal metastasis. Elife *9*, e59442. https://doi.org/10.7554/eLife.59442.

Ikeda, K., Shimizu, T., and Taguchi, R. (2008). Targeted analysis of ganglioside and sulfatide molecular species by LC/ESI-MS/MS with theoretically expanded multiple reaction monitoring. J. Lipid Res. *49*, 2678–2689. https://doi.org/10.1194/jlr.D800038-JLR200.

Iwanicki, M.P., Davidowitz, R.A., Ng, M.R., Besser, A., Muranen, T., Merritt, M., Danuser, G., Ince, T.A., Ince, T., and Brugge, J.S. (2011). Ovarian cancer spheroids use myosin-generated force to clear the mesothelium. Cancer Discov. *1*, 144–157. https://doi.org/10.1158/2159-8274.CD-11-0010.

Jacob, F., Alam, S., Konantz, M., Liang, C.-Y., Kohler, R.S., Everest-Dass, A.V., Huang, Y.-L., Rimmer, N., Fedier, A., Schötzau, A., et al. (2018). Transition of mesenchymal and epithelial cancer cells depends on α1-4 galactosyltransferase-mediated glycosphingolipids. Cancer Res. *78*, 2952–2965. https://doi.org/10.1158/0008-5472.CAN-17-2223.

Jaques, L.W., Brown, E.B., Barrett, J.M., and Brey WS Jr Weltner, W., Jr. (1977). Sialic acid. A calcium-binding carbohydrate. J. Biol. Chem. *252*, 4533–4538.

Karacosta, L.G., Anchang, B., Ignatiadis, N., Kimmey, S.C., Benson, J.A., Shrager, J.B., Tibshirani, R., Bendall, S.C., and Plevritis, S.K. (2019). Mapping lung cancer epithelial-mesenchymal transition states and trajectories with single-cell resolution. Nat. Commun. *10*, 5587. https://doi.org/10.1038/s41467-019-13441-6.

Karnoub, A.E., Dash, A.B., Vo, A.P., Sullivan, A., Brooks, M.W., Bell, G.W., Richardson, A.L., Polyak, K., Tubo, R., and Weinberg, R.A. (2007). Mesenchymal stem cells within tumour stroma promote breast cancer metastasis. Nature *449*, 557–563. https://doi.org/10.1038/nature06188.

Kinker, G.S., Greenwald, A.C., Tal, R., Orlova, Z., Cuoco, M.S., McFarland, J.M., Warren, A., Rodman, C., Roth, J.A., Bender, S.A., et al. (2020). Pan-cancer single-cell RNA-seq identifies recurring programs of cellular heterogeneity. Nat. Genet. *52*, 1208–1218. https://doi.org/10.1038/s41588-020-00726-6.

Kogiso, H., Hosogi, S., Ikeuchi, Y., Tanaka, S., Shimamoto, C., Matsumura, H., Nakano, T., Sano, K.-I., Inui, T., Marunaka, Y., and Nakahari, T. (2017). A low [Ca2+]i-induced enhancement of cAMP-activated ciliary beating by PDE1A inhibition in mouse airway cilia. Pflugers Arch. *469*, 1215–1227. https://doi.org/10.1007/s00424-017-1988-9.

Kovbasnjuk, O., Mourtazina, R., Baibakov, B., Wang, T., Elowsky, C., Choti, M.A., Kane, A., and Donowitz, M. (2005). The glycosphingolipid globotriaosylceramide in the metastatic transformation of colon cancer. Proc. Natl. Acad. Sci. USA *102*, 19087–19092. https://doi.org/10.1073/pnas.0506474102.

Krauss, J., Astrinidis, P., Astrinides, P., Frohnhöfer, H.G., Walderich, B., and Nüsslein-Volhard, C. (2013). transparent, a gene affecting stripe formation in Zebrafish, encodes the mitochondrial protein Mpv17 that is required for iridophore survival. Biol. Open *2*, 703–710. https://doi.org/10.1242/bio.20135132.

Lambert, A.W., Pattabiraman, D.R., and Weinberg, R.A. (2017). Emerging biological principles of metastasis. Cell *168*, 670–691. https://doi.org/10.1016/j.cell.2016.11.037.

Lau, H.Y., Tang, J., Casey, P.J., and Wang, M. (2021). Evaluating the epithelial-mesenchymal program in human breast epithelial cells cultured in soft agar using a novel macromolecule extraction protocol. Cancers *13*, 807. https://doi.org/10.3390/cancers13040807.

Liang, Y.-J., Ding, Y., Levery, S.B., Lobaton, M., Handa, K., and Hakomori, S.i. (2013). Differential expression profiles of glycosphingolipids in human breast cancer stem cells vs. cancer non-stem cells. Proc. Natl. Acad. Sci. USA *110*, 4968–4973. https://doi.org/10.1073/pnas.1302825110.

Lin, R.-J., Kuo, M.-W., Yang, B.-C., Tsai, H.-H., Chen, K., Huang, J.-R., Lee, Y.-S., Yu, A.L., and Yu, J. (2020). B3GALT5 knockout alters glycosphingolipid profile and facilitates transition to human naïve pluripotency. Proc. Natl. Acad. Sci. USA *117*, 27435–27444. https://doi.org/10.1073/pnas.2003155117.

Liu, L., Wu, N., Wang, Y., Zhang, X., Xia, B., Tang, J., Cai, J., Zhao, Z., Liao, Q., and Wang, J. (2019). TRPM7 promotes the epithelial-mesenchymal transition in ovarian cancer through the calcium-related PI3K/AKT oncogenic signaling. J. Exp. Clin. Cancer Res. *38*, 106. https://doi.org/10.1186/s13046-019-1061-y.

Martinez, C., Hofmann, T.J., Marino, R., Dominici, M., and Horwitz, E.M. (2007). Human bone marrow mesenchymal stromal cells express the neural ganglioside GD2: a novel surface marker for the identification of MSCs. Blood *109*, 4245–4248. https://doi.org/10.1182/blood-2006-08-039347.

McCarthy, D.J., Campbell, K.R., Lun, A.T.L., and Wills, Q.F. (2017). Scater: pre-processing, quality control, normalization and visualization of single-cell RNA-seq data in R. Bioinformatics *33*, 1179–1186. https://doi.org/10.1093/bioinformatics/btw777.

Meisenbichler, C., Doppler, C., Bernhard, D., and Müller, T. (2019). Improved matrix coating for positive- and negative-ion-mode MALDI-TOF imaging of lipids in blood vessel tissues. Anal. Bioanal. Chem. *411*, 3221–3227. https://doi.org/10.1007/s00216-019-01826-x.

Mereiter, S., Balmaña, M., Campos, D., Gomes, J., and Reis, C.A. (2019). Glycosylation in the era of cancer-targeted therapy: where are we heading? Cancer Cell *36*, 6–16. https://doi.org/10.1016/j.ccell.2019.06.006.

Merrill, A.H. (2011). Sphingolipid and glycosphingolipid metabolic pathways in the era of sphingolipidomics. Chem. Rev. *111*, 6387–6422. https://doi.org/10.1021/cr2002917.

Mischak, H., Seitz, T., Janosch, P., Eulitz, M., Steen, H., Schellerer, M., Philipp, A., and Kolch, W. (1996). Negative regulation of Raf-1 by phosphorylation of serine 621. Mol. Cell Biol. *16*, 5409–5418. https://doi.org/10.1128/MCB.16.10.5409.

Miše, B.P., Telesmanić, V.D., Tomić, S., Šundov, D., Čapkun, V., and Vrdoljak, E. (2015). Correlation between E-cadherin immunoexpression and efficacy of first line platinum-based chemotherapy in advanced high grade serous ovarian cancer. Pathol. Oncol. Res. *21*, 347–356. https://doi.org/10.1007/s12253-014-9827-1.

Na, T.-Y., Schecterson, L., Mendonsa, A.M., and Gumbiner, B.M. (2020). The functional activity of E-cadherin controls tumor cell metastasis at multiple steps. Proc. Natl. Acad. Sci. USA *117*, 5931–5937. https://doi.org/10.1073/pnas.1918167117.

Nguyen, K., Yan, Y., Yuan, B., Dasgupta, A., Sun, J., Mu, H., Do, K.-A., Ueno, N.T., Andreeff, M., and Battula, V.L. (2018). ST8SIA1 regulates tumor growth and metastasis in TNBC by activating the FAK-AKT-mTOR signaling pathway. Mol. Cancer Ther. *17*, 2689–2701. https://doi.org/10.1158/1535-7163.MCT-18-0399.

Ohkawa, Y., Zhang, P., Momota, H., Kato, A., Hashimoto, N., Ohmi, Y., Bhuiyan, R.H., Farhana, Y., Natsume, A., Wakabayashi, T., et al. (2021). Lack of GD3 synthase (St8sia1) attenuates malignant properties of gliomas in genetically engineered mouse model. Cancer Sci. *112*, 3756–3768. https://doi.org/10.1111/cas.15032.

Okada, T., Sinha, S., Esposito, I., Schiavon, G., López-Lago, M.A., Su, W., Pratilas, C.A., Abele, C., Hernandez, J.M., Ohara, M., et al. (2015). The Rho GTPase Rnd1 suppresses mammary tumorigenesis and EMT by restraining Ras-MAPK signalling. Nat. Cell Biol. *17*, 81–94. https://doi.org/10.1038/ncb3082.

Park, S.-Y., Kwak, C.-Y., Shayman, J.A., and Kim, J.H. (2012). Globoside promotes activation of ERK by interaction with the epidermal growth factor receptor. Biochim. Biophys. Acta *1820*, 1141–1148. https://doi.org/10.1016/j.bbagen.2012.04.008.

Pastushenko, I., and Blanpain, C. (2019). EMT transition states during tumor progression and metastasis. Trends Cell Biol. *29*, 212–226. https://doi.org/10.1016/j.tcb.2018.12.001.

Pastushenko, I., Brisebarre, A., Sifrim, A., Fioramonti, M., Revenco, T., Boumahdi, S., Van Keymeulen, A., Brown, D., Moers, V., Lemaire, S., et al. (2018). Identification of the tumour transition states occurring during EMT. Nature *556*, 463–468. https://doi.org/10.1038/s41586-018-0040-3.

Pattabiraman, D.R., Bierie, B., Kober, K.I., Thiru, P., Krall, J.A., Zill, C., Reinhardt, F., Tam, W.L., and Weinberg, R.A. (2016). Activation of PKA leads to mesenchymal-to-epithelial transition and loss of tumor-initiating ability. Science *351*, aad3680. https://doi.org/10.1126/science.aad3680.

Pei, D., Shu, X., Gassama-Diagne, A., and Thiery, J.P. (2019). Mesenchymal-epithelial transition in development and reprogramming. Nat. Cell Biol. *21*, 44–53. https://doi.org/10.1038/s41556-018-0195-z.

Qin, C.-D., Ma, D.-N., Zhang, S.-Z., Zhang, N., Ren, Z.-G., Zhu, X.-D., Jia, Q.-A., Chai, Z.-T., Wang, C.-H., Sun, H.-C., and Tang, Z.Y. (2018). The Rho GTPase Rnd1 inhibits epithelial-mesenchymal transition in hepatocellular carcinoma and is a favorable anti-metastasis target. Cell Death Dis. *9*, 486. https://doi.org/10.1038/s41419-018-0517-x.

Rokutan, H., Hosoda, F., Hama, N., Nakamura, H., Totoki, Y., Furukawa, E., Arakawa, E., Ohashi, S., Urushidate, T., Satoh, H., et al. (2016). Comprehensive mutation profiling of mucinous gastric carcinoma. J. Pathol. *240*, 137–148. https://doi.org/10.1002/path.4761.

Rossdam, C., Konze, S.A., Oberbeck, A., Rapp, E., Gerardy-Schahn, R., von Itzstein, M., and Buettner, F.F.R. (2019). Approach for profiling of glycosphingolipid glycosylation by multiplexed capillary gel electrophoresis coupled to laser-induced fluorescence detection to identify cell-surface markers of human pluripotent stem cells and derived cardiomyocytes. Anal. Chem. *91*, 6413–6418. https://doi.org/10.1021/acs.analchem.9b01114.

Ruh, H., Sandhoff, R., Meyer, B., Gretz, N., and Hopf, C. (2013). Quantitative characterization of tissue globotetraosylceramides in a rat model of polycystic kidney disease by PrimaDrop sample preparation and indirect high-performance thin layer chromatography-matrix-assisted laser desorption/ionization-time-of-flight-mass spectrometry with automated data acquisition. Anal. Chem. *85*, 6233–6240. https://doi.org/10.1021/ac400931u.

Säljö, K., Barone, A., Vizlin-Hodzic, D., Johansson, B.R., Breimer, M.E., Funa, K., and Teneberg, S. (2017). Comparison of the glycosphingolipids of human-induced pluripotent stem cells and human embryonic stem cells. Glycobiology *27*, 291–305. https://doi.org/10.1093/glycob/cww125.

Santin, A.D., Ravindranath, M.H., Bellone, S., Muthugounder, S., Palmieri, M., O'Brien, T.J., Roman, J., Cannon, M.J., and Pecorelli, S. (2004). Increased levels of gangliosides in the plasma and ascitic fluid of patients with advanced ovarian cancer. BJOG *111*, 613–618. https://doi.org/10.1111/j.1471-0528.2004.00142.x.

Sarkar, T.R., Battula, V.L., Werden, S.J., Vijay, G.V., Ramirez-Peña, E.Q., Taube, J.H., Chang, J.T., Miura, N., Porter, W., Sphyris, N., et al. (2015). GD3 synthase regulates epithelial-mesenchymal transition and metastasis in breast cancer. Oncogene *34*, 2958–2967. https://doi.org/10.1038/onc.2014.245.

Sawada, K., Mitra, A.K., Radjabi, A.R., Bhaskar, V., Kistner, E.O., Tretiakova, M., Jagadeeswaran, S., Montag, A., Becker, A., Kenny, H.A., et al. (2008). Loss of E-cadherin promotes ovarian cancer metastasis via alpha 5-integrin, which is a therapeutic target. Cancer Res. *68*, 2329–2339. https://doi.org/10.1158/0008-5472.CAN-07-5167.

Schjoldager, K.T., Narimatsu, Y., Joshi, H.J., and Clausen, H. (2020). Global view of human protein glycosylation pathways and functions. Nat. Rev. Mol. Cell Biol. *21*, 729–749. https://doi.org/10.1038/s41580-020-00294-x.

Schliekelman, M.J., Taguchi, A., Zhu, J., Dai, X., Rodriguez, J., Celiktas, M., Zhang, Q., Chin, A., Wong, C.-H., Wang, H., et al. (2015). Molecular portraits of epithelial, mesenchymal, and hybrid States in lung adenocarcinoma and their relevance to survival. Cancer Res. *75*, 1789–1800. https://doi.org/10.1158/0008-5472.CAN-14-2535.

Schnaar, R.L., and Kinoshita, T. (2015). Glycosphingolipids. In Essentials of Glycobiology, A. Varki, R.D. Cummings, J.D. Esko, P. Stanley, G.W. Hart, M. Aebi, A.G. Darvill, T. Kinoshita, N.H. Packer, and J.H. Prestegard, et al., eds. (Cold Spring Harbor Laboratory Press).

Shi, M., Whorton, A.E., Sekulovski, N., Paquet, M., MacLean, J.A., Song, Y., Van Dyke, T., and Hayashi, K. (2020). Inactivation of TRP53, PTEN, RB1, and/or CDH1 in the ovarian surface epithelium induces ovarian cancer transformation and metastasis. Biol. Reprod. *102*, 1055–1064. https://doi.org/10.1093/biolre/ioaa008.

Song, Y., Ye, M., Zhou, J., Wang, Z.-W., and Zhu, X. (2019). Restoring E-cadherin expression by natural compounds for anticancer therapies in genital and urinary cancers. Mol. Ther. Oncolytics *14*, 130–138. https://doi.org/10.1016/j.omto.2019.04.005.

Tan, T.Z., Miow, Q.H., Miki, Y., Noda, T., Mori, S., Huang, R.Y.-J., and Thiery, J.P. (2014). Epithelial-mesenchymal transition spectrum quantification and its efficacy in deciphering survival and drug responses of cancer patients. EMBO Mol. Med. *6*, 1279–1293. https://doi.org/10.15252/emmm.201404208.

Theruvath, J., Menard, M., Smith, B.A.H., Linde, M.H., Coles, G.L., Dalton, G.N., Wu, W., Kiru, L., Delaidelli, A., Sotillo, E., et al. (2022). Anti-GD2 synergizes with CD47 blockade to mediate tumor eradication. Nat. Med. *28*, 333–344. https://doi.org/10.1038/s41591-021-01625-x.

Tian, X., Liu, Z., Niu, B., Zhang, J., Tan, T.K., Lee, S.R., Zhao, Y., Harris, D.C.H., and Zheng, G. (2011). E-cadherin/β-catenin complex and the epithelial barrier. J. Biomed. Biotechnol. *2011*, 567305. https://doi.org/10.1155/2011/567305.

Treindl, F., Ruprecht, B., Beiter, Y., Schultz, S., Döttinger, A., Staebler, A., Joos, T.O., Kling, S., Poetz, O., Fehm, T., et al. (2016). A bead-based western for high-throughput cellular signal transduction analyses. Nat. Commun. *7*, 12852. https://doi.org/10.1038/ncomms12852.

Villalonga, P., and Ridley, A.J. (2006). Rho GTPases and cell cycle control. Growth Factors *24*, 159–164.

Wan, H., Li, Z., Wang, H., Cai, F., and Wang, L. (2021). ST8SIA1 inhibition sensitizes triple negative breast cancer to chemotherapy via suppressing Wnt/β-catenin and FAK/Akt/mTOR. Clin. Transl. Oncol. *23*, 902–910. https://doi.org/10.1007/s12094-020-02484-7.

Xing, P., Wang, Y., Zhang, L., Ma, C., and Lu, J. (2021). Knockdown of lncRNA MIR4435-2HG and ST8SIA1 expression inhibits the proliferation, invasion and migration of prostate cancer cells in vitro and in vivo by blocking the activation of the FAK/AKT/β-catenin signaling pathway. Int. J. Mol. Med. *47*, 93. https://doi.org/10.3892/ijmm.2021.4926.

Xu, J., Liao, W., Gu, D., Liang, L., Liu, M., Du, W., Liu, P., Zhang, L., Lu, S., Dong, C., et al. (2009). Neural ganglioside GD2 identifies a subpopulation of mesenchymal stem cells in umbilical cord. Cell. Physiol. Biochem. *23*, 415–424. https://doi.org/10.1159/000218188.

Yamashita, N., Tokunaga, E., Iimori, M., Inoue, Y., Tanaka, K., Kitao, H., Saeki, H., Oki, E., and Maehara, Y. (2018). Epithelial paradox: clinical significance of coexpression of E-cadherin and vimentin with regard to invasion and metastasis of breast cancer. Clin. Breast Cancer *18*, e1003–e1009. https://doi.org/10.1016/j.clbc.2018.02.002.

Yao, D., Dai, C., and Peng, S. (2011). Mechanism of the mesenchymal-epithelial transition and its relationship with metastatic tumor formation. Mol. Cancer Res. *9*, 1608–1620. https://doi.org/10.1158/1541-7786.MCR-10-0568.

Yu, A.L., Gilman, A.L., Ozkaynak, M.F., London, W.B., Kreissman, S.G., Chen, H.X., Smith, M., Anderson, B., Villablanca, J.G., Matthay, K.K., et al. (2010). Anti-GD2 antibody with GM-CSF, interleukin-2, and isotretinoin for neuroblastoma. N. Engl. J. Med. *363*, 1324–1334. https://doi.org/10.1056/NEJMoa0911123.

Yu, G., and He, Q.-Y. (2016). ReactomePA: an R/Bioconductor package for reactome pathway analysis and visualization. Mol. Biosyst. *12*, 477–479. https://doi.org/10.1039/c5mb00663e.

Zhang, T., van Die, I., Tefsen, B., van Vliet, S.J., Laan, L.C., Zhang, J., Ten Dijke, P., Wuhrer, M., and Belo, A.I. (2020). Differential O- and glycosphingolipid glycosylation in human pancreatic adenocarcinoma cells with opposite morphology and metastatic behavior. Front. Oncol. *10*, 732. https://doi.org/10.3389/fonc.2020.00732.

Zheng, X., Carstens, J.L., Kim, J., Scheible, M., Kaye, J., Sugimoto, H., Wu, C.-C., LeBleu, V.S., and Kalluri, R. (2015). Epithelial-to-mesenchymal transition is dispensable for metastasis but induces chemoresistance in pancreatic cancer. Nature *527*, 525–530. https://doi.org/10.1038/nature16064.

STAR★METHODS

KEY RESOURCES TABLE

REAGENT or RESOURCE	SOURCE	IDENTIFIER
Antibodies		
Rabbit monoclonal anti-E-Cadherin (24E10)	Cell Signaling Technology	Cat# 3195; RRID:AB_2291471
Rabbit monoclonal anti-E-cadherin (EP700Y)	Sigma-Aldrich (Ventana)	Cat# MA5-14458; RRID:AB_10981095
Rabbit polyclonal anti-GFP	GeneTex	Cat# GTX113617; RRID:AB_1950371
Mouse monoclonal anti-Vimentin	Thermo Fisher Scientific	Cat# MA5-11883; RRID:AB_10985392
Mouse monoclonal anti-EpCAM (VU1D9)	Cell Signaling Technology	Cat# 2929; RRID:AB_2098657
Rabbit monoclonal anti-Claudin 1 (D3H7C)	Cell Signaling Technology	Cat# 13995; RRID:AB_2798358
Rabbit monoclonal anti-Claudin 3 (D7A3O)	Cell Signaling Technology	Cat# 83609; RRID:AB_2800021
Rabbit monoclonal anti-β-Catenin (D10A8) XP	Cell Signaling Technology	Cat# 8480; RRID:AB_11127855
Rabbit monoclonal anti-SNAIL (C15D3)	Cell Signaling Technology	Cat# 3879; RRID:AB_2255011
Rabbit monoclonal anti-Slug (C19G7)	Cell Signaling Technology	Cat# 9585;, RRID:AB_2239535
Mouse monoclonal GAPDH (0411)	Santa Cruz Biotechnology	Car# sc-47724; RRID:AB_627678
Rabbit monoclonal anti-alpha/beta-Tubulin	Cell Signaling Technology	Cat# 2148; RRID:AB_2288042
Rabbit monoclonal anti-N-Cadherin (D4R1H)	Cell Signaling Technology	Cat# 13116; RRID:AB_2687616
Rabbit monoclonal anti-Cyclin D1 (92G2)	Cell Signaling Technology	Cat# 2978; RRID:AB_2259616
Rabbit polyclonal anti-p27 Kip1	Cell Signaling Technology	Cat# 2552; RRID:AB_10693314
Mouse monoclonal anti-Cas9 (7A9-3A3)	Cell Signaling Technology	Cat# 14697; RRID:AB_2750916
Rabbit polyclonal anti-mTOR	GeneTex	Cat# GTX30346; RRID:AB_385473
Rabbit monoclonal anti-mTOR phospho-S2448 (D9C2)	Cell Signaling Technology	Cat# 5536, RRID:AB_10691552
Rabbit monoclonal anti-EGFR (D38B1)	Cell Signaling Technology	Cat# 4267; RRID:AB_2246311
Rabbit monoclonal anti-EGFR phospho-T669 (D2F1)	Cell Signaling Technology	Cat# 8808; RRID:AB_11179086
Rabbit monoclonal anti-EGFR phospho-Y1068 (D7A5) XP	Cell Signaling Technology	Cat# 14565; RRID:AB_2798512
Mouse monoclonal (pan) anti-AKT (40D4)	Cell Signaling Technology	Cat# 2920; RRID:AB_1147620
Rabbit monoclonal anti-AKT1 phospho-S124 (EPR17680)	Abcam	Cat#ab183556; RRID: N/A
Rabbit monoclonal anti-p44/42 MAPK (Erk1/2)	Cell Signaling Technology	Cat# 9102; RRID:AB_330744
Rabbit monoclonal anti-phospho p44/p42 MAPK Y202/T204 (D13.14.4E)	Cell Signaling Technology	Cat# 4370; RRID:AB_2315112
Rabbit monoclonal anti-phospho β-catenin (Ser552) (D8E11)	Cell Signaling Technology	Cat# 5651; RRID:AB_10831053
IgM anti-Gb3/CD77	Bio-Rad	Cat# MCA570; RRID: N/A
IgM anti-SSEA3 (eBioMC-631)	eBioscience	Cat# 13-8833-82; RRID:AB_657842
IgM anti-SSEA4 (eBioMC-813-70)	eBioscience	Cat# 14-8843-80; RRID: AB_657847
IgG3 anti-GloboH (Vk9)	eBioscience	Cat# 14-9700-80; RRID:AB_2572960
IgM anti-nLc4 IgM	PMID: 7287743	N/A
IgM anti-P1 (P3NIL100)	Millipore	Cat# ND-1L-BK; RRID: N/A
FITC Mouse anti-Human Disialoganglioside GD2 (14.G2a)	BD Bioscience	Cat# 563439, RRID:AB_2738206
IgG3 anti-GD3 (MB3.6)	BD Bioscience	Cat# 554274; RRID:AB_395338
anti GM1-FITC	Sigma Aldrich	Cat# C1655; RRID: N/A
Biotin Rat anti-Mouse IgG2b (R12-3)	BD Bioscience	Cat# 553393; RRID:AB_394831
Biotin Mouse anti-Rat IgM (G53-238)	BD Bioscience	Cat# 553886; RRID:AB_395115
Biotin Rat anti-Mouse IgM (II/41)	BD Bioscience	Cat# 553436; RRID:AB_394856
Biotin Mouse anti-Human IgM (G20-127)	BD Bioscience	Cat# 555781; RRID:AB_396116
FITC-Streptavidin	BD Bioscience	Cat# 554060; RRID:AB_10053373
PE-Cy7™ Mouse anti-Human CD24 (ML5)	BD Bioscience	Cat# 561646; RRID:AB_10892826

(Continued on next page)

Continued

REAGENT or RESOURCE	SOURCE	IDENTIFIER
PE Mouse anti-Human CD44 (515)	BD Bioscience	Cat# 550989; RRID:AB_394000
APC/Cy7 anti-Human CD45 (HI30)	BD Bioscience	Cat# 304014; RRID:AB_314402
Bacterial and virus strains		
One Shot™ Stbl3™ Chemically Competent *E. coli*	ThermoFisher Scientific	Cat# C737303
*S*ubcloning Efficiency™ DH5α Competent Cells	ThermoFisher Scientific	Cat# 18265017
Chemicals, peptides, and recombinant proteins		
DAPI	BD Bioscience	Cat# 564907
Pierce™ BCA Protein Assay Kit	ThermoFisher Scientific	Cat# 23225
ProLong® Gold antifade reagent	Cell Signaling Technology	Cat# 9071
Radioimmunoprecipitation assay buffer (RIPA)	Cell Signaling Technology	Cat# 9806
Thiazolyl Blue Tetrazolium Bromide (MTT)	Sigma-Aldrich	Cat# M2128
Agarose, low gelling temperature	Sigma-Aldrich	Cat# A9414
Fetal Bovine Serum	Sigma-Aldrich	Cat# F7524
Bovine serum albumin	Sigma-Aldrich	Cat# A9418
Proteinase Inhibitor Cocktails	Sigma-Aldrich	Cat# P8340
Cell-dissociation solution non-enzymatic	Sigma-Aldrich	Cat# C5914
JetPEI DNA transfection reagent	Polyplus-transfection	Cat# 101-10N
Accutase® Solution	Sigma-Aldrich	Cat# A6964
Collagenase/Dispase	Sigma-Aldrich	Cat# 10269638001
DNAse I (RNase-free)	BioLabs (NEB)	Cat# M0303S
Red Blood Cell lysis	Miltenyi Biotec	Cat# 130-094-183
Alexa Fluor® 647 Phalloidin	Cell Signaling Technology	Cat# 8940
DMEM (1×) Without Calcium	ThermoFisher Scientific	Cat# 21068028
BAPTA-AM	Abcam	Cat# ab120503
Calcium chloride Dihydrate	Carl Roth	Cat# HN04.1
EGTA	Sigma-Aldrich	Cat# E4378
CellTracker™CM-Dil Dye	ThermoFisher Scientific	Cat# C7000
1,5-Diaminonaphthalene (DAN)	Sigma-Aldrich	Cat# 56451
Ammonium formate	Sigma-Aldrich	Cat# 70221
Acetonitrile	Sigma-Aldrich	Cat# 1000292500
Formic acid	Sigma-Aldrich	Cat# 00940
Experimental models: Cell lines		
SK-OV-3	ATCC	RRID:CVCL_0532
SKOV3.ip1	ATCC	RRID:CVCL_0C84
TOV-112D	ATCC	RRID:CVCL_3612
BG1	Oncotest GmbH	RRID:CVCL_6571
OVCAR-3	ATCC	RRID:CVCL_0465
OVCAR-4	Charles River Laboratories	RRID:CVCL_1627
Kuramochi	JCRB	RRID: CVCL_1345
OAW42	ECACC	RRID:CVCL_1615
IGROV-1	ATCC	RRID:CVCL_1304
A2780	ATCC	RRID:CVCL_0134
Tyk-nu	JCRB	RRID:CVCL_1776
HEK293T		RRID:CVCL_0045
SKOV3 knock-out *ST8SIA1* (PX458)	This paper	N/A
SKOV3 knock-out *A4GALT* (PX458)	PMID: 29572228	N/A
SKOV3ip knock-out *ST8SIA1* (CRISPRv2)	This paper	N/A
TOV-112D knock-out *ST8SIA1* (CRISPRv2)	This paper	N/A
SKOV3ip knock-out *AAVS1* (CRISPRv2)	This paper	N/A

Continued

REAGENT or RESOURCE	SOURCE	IDENTIFIER
TOV-112D knock-out *AAVS1* (CRISPRv2)	This paper	N/A
BG1 CRISPR-*Cas9*-mediated knock-in (clone STOP)	This paper	N/A
BG1 CRISPR-*Cas9*-mediated knock-in (clone −60)	This paper	N/A
BG1 CRISPR-*Cas9*-mediated knock-in (clone −171)	This paper	N/A
Experimental models: Organisms/strains		
Zebrafish Tg(kdrl:eGFP)	PMID: 17306248	la116tg
Oligonucleotides		
ST8SIA1-for1 (PCR): ACAAGCAAGAAGGGCAAGAA	This paper	N/A
ST8SIA1-rev1 (PCR): CGAGTCTTTACATGCGCAAA	This paper	N/A
ST8SIA1-for2 (PCR): CGTGCGTTTGCAAGTAAGAG	This paper	N/A
ST8SIA1-rev2 (PCR): AACTTCCACGCCAGTACAGC	This paper	N/A
sgRNA1_*ST8SIA1*_F1: caccgCGCGGCTCGGATCGGGTCGA	This paper	N/A
sgRNA1_*ST8SIA1*_R1: aaacTCGACCCGATCCGAGCCGCGc	This paper	N/A
sgRNA2_*ST8SIA1*_F2: caccgCGCCTTGCACCGTCTCGCAG	This paper	N/A
sgRNA2_*ST8SIA1*_R2: aaacCTGCGAGACGGTGCAAGGCGc	This paper	N/A
sgRNA1_*AAVS1*_F1: caccgACTGTTGACGGCGGCGATGT	This paper	N/A
sgRNA2_*AAVS1*_R1: aaacACATCGCCGCCGTCAACAGT	This paper	N/A
sgRNA CDH1_STOP_F1: ACACCTGACATGTACGGAGGCGGCGG	This paper	N/A
sgRNA CDH1_STOP_R1: AAAACCGCCGCCTCCGTACATGTCAG	This paper	N/A
sgRNA CDH1_-60_F1: ACACCACTATGACTACTTGAACGAAG	This paper	N/A
sgRNA CDH1_-60_R1: AAAACTTCGTTCAAGTAGTCATAGTG	This paper	N/A
sgRNA CDH1_-171_F1: ACACCACGAGCAGAGAATCATAAGGG	This paper	N/A
sgRNA CDH1_-171_R1: AAAACCCTTATGATTCTCTGCTCGTG	This paper	N/A
CDH1_PCR_F1: AGCCCCACTCTGATCTATGG	This paper	N/A
CDH1_PCR_R1: GGGACACACCAGTGTAGTAATGA	This paper	N/A
EGFP-C_F CATGGTCCTGCTGGAGTTCGTG	This paper	N/A
EGFP-N_R CGTCGCCGTCCAGCTCGACCAG	This paper	N/A
Recombinant DNA		
pCMVR8.74	Addgene	RRID:Addgene_22036
pMD2.G	Addgene	RRID:Addgene_12259
lentiCRISPRv2	Addgene	RRID:Addgene_52961
pSpCas9(BB)-2A-GFP	Addgene	RRID:Addgene_48138
pSpCas9(BB)-2A-GFP_*ST8SIA1*-sgRNA1	This paper	N/A
pSpCas9(BB)-2A-GFP_*ST8SIA1*-sgRNA2	This paper	N/A
pSpCas9(BB)-2A-GFP_*A4GALT*-sgRNA1	This paper	N/A

(Continued on next page)

Continued

REAGENT or RESOURCE	SOURCE	IDENTIFIER
pSpCas9(BB)-2A-GFP_*A4GALT*-sgRNA2	This paper	N/A
lentiCRISPRv2-*ST8SIA1*-sgRNA1	This paper	N/A
lentiCRISPRv2-*ST8SIA1*-sgRNA2	This paper	N/A
lentiCRISPRv2-*AAVS1*-sgRNA1	This paper	N/A
lentiCRISPRv2-*AAVS1*-sgRNA2	This paper	N/A
MLM3636	Addgene	RRID:Addgene_43860
hCas9	Addgene	RRID:Addgene_41815
Sg-A	Addgene	RRID:Addgene_83807
double cut NH-donor	Addgene	RRID:Addgene_83576
sgRNA CDH1_STOP_EGPF_MLM3636	This paper	N/A
sgRNA CDH1_-171_1_MLM3636	This paper	N/A
sgRNA CDH1_-60_1_MLM3636	This paper	N/A
Software and algorithms		
R studio 4.0.3	R Core Team, 2017	https://www.R-project.org/
GraphPad Prism 9	Pad Software, Inc.	https://www.graphpad.com/
ImageJ	NIH	https://imagej.nih.gov/ij/
FlowJo v10	Becton Dickinson	https://www.flowjo.com/
Image Lab 6.0.1	Bio-Rad	https://www.bio-rad.com/
HALO Image Analysis	Indica Labs	https://indicalab.com
ReactomePA	Yu and He (2016)	NA
OMERO v5.6	OME project	https://www.openmicroscopy.org/omero
SCILs Lab	Bruker	https://scils.de
Flex-Control	Bruker	https://www.bruker.com/en.html
FlexAnalysis Batch Process	Bruker	https://www.bruker.com/en.html
Metabolomics Workbench	UCSD	https://www.metabolomicsworkbench.org
Lipid-Maps	UCSD	https://www.lipidmaps.org
Adobe Illustrator 2021	Adobe	https://www.adobe.com/ch_de/?mv=search&sdid=88X75SKX
ComplexHeatmap	Bioconductor	https://www.bioconductor.org
BiocManager	Bioconductor	https://www.bioconductor.org
DGE List (R package edgeR)	Bioconductor	https://www.bioconductor.org
Rgraphviz	Bioconductor	https://www.bioconductor.org
pcaMethods	Bioconductor	https://www.bioconductor.org
CompareGroups	CRAN	https://cran.r-project.org
tabplot	CRAN	https://cran.r-project.org
tidyverse	CRAN	https://cran.r-project.org
ggplot2	CRAN	https://cran.r-project.org
XLConnectJars	CRAN	https://cran.r-project.org

RESOURCE AVAILABILITY

Lead contact
Further information and requests for resources should be directed to and will be fulfilled by the lead contact, Francis Jacob (francis.jacob@unibas.ch).

Materials availability
All relevant data supporting the key findings of this study are available within the article and its supplementary information or from the corresponding authors upon reasonable request.

Data and code availability

- Publicly available data were reanalyzed in this study: Kinker et al.: GSE157220), Tothill et al.: GSE9899, TCGA: GSE62944, Bild et al.: GSE3149, Anglesio et al.: GSE48351, and Denker et al.: GSE14764)
- R packages used in the work are listed in the STAR Methods section/Method details
- Any additional information required to reanalyze the data reported in this work is available from the lead contact upon request

EXPERIMENTAL MODEL AND SUBJECT DETAILS

Patient-derived tissue
Tissue microarrays
The current study utilised two independent cohorts, 1) an Australian cohort consisting of patients' tissue samples obtained from primary and metastatic tumour sites (Tables S1) and S2) a Swiss longitudinal patient cohort with tissue samples collected at different time points (Table S2). Ethical approval and written informed consent were granted for sampling and anonymised collection of clinicopathological patient data at different sites in Australia (Gynaecological Cancer Centre, Royal Hospital for Women, Sydney: HREC 16/04/20/5.06 and 2019/ETH00918, to V.H.S.) and Switzerland (University Hospital Basel: EKNZ: 2017–01900, to V.H.S). Haematoxylin & Eosin (H&E) stained sections of each sample from both cohorts were reviewed by a pathologist specialised in gynaecological pathology (T.V. for Swiss and James P. Scurry for Australian cohort) and areas corresponding to tumour/benign tissue marked. Each patient was represented by at least two cores sampled from different areas of the tumour. Patients with a past history of cancer or inflammatory/autoimmune diseases were excluded from this study.

Slow-frozen tissue samples for GSL expression determined by flow cytometry
Additional slow-frozen samples derived from either chemo-naive, neoadjuvant, or recurrent high-grade OC patients (n = 19 samples from 17 patients) were taken from our biobank for flow cytometry analysis using CD45 to gate out lymphocytes and DAPI to remove dead cells. Slow-frozen samples were enzymatically dissociated as described in the patient-derived OC sample dissociation section.

Snap-frozen tissue samples for MALDI imaging
The spatial distribution of GSLs were investigated using MALDI imaging on additional snap-frozen and matched tissue samples derived from chemo-naive, advanced FIGO stage, and high-grade serous ovarian cancer patients (n = 9 patients with 17 samples in total). The sample cohort consisted of the primary tumour (either ovary or fallopian tube) and metastasis (omentum).

Cell lines
All cell lines used in the study are listed in the key resources table.

METHOD DETAILS

Immunohistochemistry
Tissue microarrays were prepared according to a standard protocol. Briefly, formalin-fixed and paraffin-embedded (FFPE) tissue sections were cut at 5 μm section thickness and mounted on glass slides. All sections were dried overnight at 37°C and stored at 4°C, protected from light. Paraffin was removed by different solvent washes in xylene, 100% ethanol, 95% ethanol, 70% ethanol, 50% ethanol, and water. Antigens were retrieved by boiling the tissue section in pre-boiled 10 mM Sodium citrate buffer pH6.0 in a microwave (800 W). Tissue sections were incubated in 3% hydrogen peroxide (10 min), washed in ddH$_2$O, permeabilized with 0.25% Triton X-100 in PBS (5 min) and washed with PBS. Each slide was blocked with 1% BSA, 5% FBS and 0.1% Triton X-100 in PBS (30 min), then incubated overnight with the primary antibody in 1% BSA and 0.1% Triton X-100 in PBS. The next day, tissues were washed with TBS, incubated with SignalStain Boost detection reagent for 30 min, washed with ddH$_2$O, incubated with DAB solution for 7 min, and washed with TBST.

Image analysis
TMAs stained by IHC were digitised by a Hamamatsu Nanozoomer S60 slide scanner. Digital slides were then analysed by Halo image analysis software. In short, each tissue patch of the TMA was analysed by the Random Forest algorithm for classifying stroma and tumour classes. The software was then trained for cell recognition, signal recognition and quantification. E-Cadherin expression was quantified as frequency of positive cells in each class, and staining intensity by scoring (i.e. 1, 2, 3) for each subcellular compartment. The corresponding histoscore (Hirsch et al., 2003) was also calculated.

Access to publicly available bulk transcriptomic data and analysis
Publicly available transcriptomic datasets of *curatedOvarianData* were downloaded from Gene Expression Omnibus (http://www.ncbi.nlm.nih.gov/geo/). The *curatedOvarianData* package provides a comprehensive resource of curated gene expression and clinical data for the development and validation of ovarian cancer prognostic models including hazard ratio and forest plots

(Ganzfried et al., 2013). Gene expression data for the Cancer Cell Line Encyclopaedia (CCLE) were accessed through the cBioPortal using R (www.cbioportal.org) and *cgdsr* for querying the Cancer Genomics Data Server (Barretina et al., 2012).

Analysis of single-cell RNAseq data

FASTQ data were aligned and quantified using GRCh38 reference and Cell Ranger v4.0.0 was used to perform alignment of reads, generate gene-cell matrices and perform clustering and gene expression analysis. The count matrix (Kinker et al., 2020) was downloaded from the Gene Expression Omnibus (GEO, accession number GSE157220) and metadata was downloaded from the Broad Institute's single-cell portal (SCP542). Transcript counts were normalized by using transcripts per million (TPM) normalization and normalized data were log-transformed (log_2) using a pseudo-count of 1. We used the scatter package (McCarthy et al., 2017) to obtain a 2-dimensional representation of the normalised counts using runUMAP win *min_dist* set to 0.01. Each cell is colored by the average gene expression of selected gene markers based on the following GO pathways: GO0035584 (GO_CALCIUM_ MEDIATED_INTRACELLULAR), GO0016339 (GO_ CALCIUM_DEPENDENT), GO0005544 (GO_CALCIUM_DEPENDENT_PHOS PHOLIPID), GO0010857 (GO_CALCIUM_Dependent_PKA), GO0016338 (GO_CALCIUM_INDEPENDENT), GO0019722 (GO_CAL CIUM_MEDIATED_SIGNALING), GO0060401 (GO_CYTOSOLIC_ CALCIUM_ION_TRANSPORT), GO0050849 (GO_NEGATIVE_ REGULATION_CALCIUM), GO0050850 (GO_POSITIVE_REGULATION_CALCIUM), GO 0051482 (GO_POSITIVE_ REGULATION), GO0050848 (GO_REGULATION_OF_CALCIUM_MEDIATED_SIGNALING), GO0099566 (GO_REGULATION_POSTSYNAPTIC_ CYTOSOLIC_CALCIUM), GO0099509 (GO_ REGULATION_PRESYNAPTIC), GO0006688 (GOBP_GLYCOSPHINGOLIPID_ BIOSYNTHETIC_ PROCESS)

MALDI-mass spectrometer imaging (MSI)

Tissue samples were immediately snap-frozen in liquid nitrogen and stored at $-80°C$ until further use. Tissue cryosections were prepared at 5 μm thickness for MALDI-MSI and were thaw-mounted on indium tin oxide (ITO) glass slides (Bruker Daltonics, Bremen, Germany). Prior to matrix application of the MALDI matrix, tissue sections were washed using ammonium formate (50 mM) according to standard protocol (Angel et al., 2012). This step was found to be critical to enhance detection and remove any adducts. We used 1,5-Diaminonaphthalene (DAN) as MALDI matrix, which can be used for lipid imaging analysis in both positive and negative ion mode MALDI-MS measurement (Meisenbichler et al., 2019). DAN matrix solution was prepared to 20 mg/mL in acetonitrile/water (70/30, v/v) with 0.1% formic acid. Matrix was applied using HTX TM-sprayer (3 layers, 0.1 mL/min, 40°C, velocity of 1300, crisscross pattern, 2.5 mm track spacing, nitrogen gas pressure was set to 10 psi). MALDI-MSI data were acquired using the rapifleX MALDI TOF/TOF mass spectrometer (Bruker, Daltonics) equipped with the SmartBean 3D 10 kHz laser and operated in both positive and negative-ion reflectron mode. The laser power was optimised at the start of each run and then held constant during the MALDI-MSI experiment. A total of 500 laser shots were used to acquire data at 50 μm pixel resolution for the m/z 500–2300 range at each sampling position. Spectra were normalised against (Root Mean Square) of all data points. Mass spectra analyses and chemical formula calculations were performed in flexAnalysis (Bruker Daltonics, v.4) and SCILs. After the MALDI-MSI measurements, the matrix was removed by rinsing the samples in 100% ethanol and H&E staining was performed according to a standard protocol.

Cell culture

All ovarian cancer cell lines were cultured in RPMI-1640 growth medium supplemented with 10% FBS (Sigma-Aldrich), 100 U/mL penicillin and 0.1 mg/mL streptomycin (all purchased from Sigma-Aldrich, Switzerland) at 37°C in a 95% humidified atmosphere containing 5% CO_2. All the cell lines were STR-profiled (Microsynth AG, Switzerland) and regularly tested for the absence of *Mycoplasma*.

Molecular cloning

Single guide RNAs (sgRNA) targeting exon 1 of *ST8SIA1* were designed using the Zhang laboratory's web tool (http://crispr.mit.edu). Both sgRNA1 and sgRNA2 with quality scores of 98 and 92, respectively, were selected for gene editing of *ST8SIA1* transcription start site (TSS). Both oligonucleotides were cloned into either pSpCas9(BB)-2A-GFP (addgene, #PX458, #48138) or lentiCRISPR v2 (addgene #52961) using *BsbI* restriction sites and annealed using T4-DNA ligase (Promega, Switzerland). Plasmids were transformed into either DH5alpha or Stbl3 *E.coli* strains and sequenced to confirm insertion of respective sgRNA by Sanger DNA sequencing using the human U6 primer.

Generation of homozygously deleted *ΔST8SIA1* cell lines

Cells were grown in a 6-well plate (3–5x10^5 cells/well) for 24h and transfected with PX458 (addgene #48138) containing 2.5 μg of the corresponding sgRNA using a lipofectamine transfection reagent to generate homozygous *ΔST8SIA1* in the SKOV3 cell line. Cells were washed with PBS, harvested using 1× trypsin (Sigma) and resuspended in RPMI-1640 containing 10% FBS and 1% P/S, 72h after transfection. Transient EGFP single cells were sorted with a BD FACSAria Cell Sorter (BD Bioscience) into a 96-well plate and transferred into a 48-well plate upon confluence. Genotyping PCR was performed on genomic DNA to characterise obtained and expanded clones.

Lentiviral transduction for generating *ST8SIA1* mutant cells

For preparation of lentiviral particles, HEK293T cells were seeded at 50% confluency in a T75 flask one day prior to transfection. 4 μg of lentiCRISPR v2, 2 μg of pMD2.G (addgene #12259) and 2 μg of pCMVR8.74 (addgene #22036) were co-transfected using 24 μL of jetPEI reagent in 1 mL of 150 mM NaCl solution (Polyplus-transfection, Chemie Brunschwig AG, Switzerland). Medium was changed 24h after transfection. Virus supernatant was collected 48h later and filtered with a 0.45 μm polyvinylidene fluoride filter (Sartorius AG, Germany). Transduced cells were kept under selection with a concentration of 1 μg/μL puromycin.

Genotyping PCR

Transiently transfected and transduced EGFP positive clones were selected and characterised to identify homozygous knockout by using two different PCR primer pairs. PCR was performed using 2.5× GoTaq Green Master Mix (Promega), 200 nM primers (primer-F1/primer-R1: 1836bp (wildtype) and 742bp (knockout), primer-F2/primer-R2: 198bp (wildtype)), and 100 μg genomic DNA (gDNA). PCR conditions were 95°C for 1 min, 56°C for 15 s, 72°C for 90 s, and finished with 1 cycle at 72°C for 5 min. Amplicons were visualised on a 1.5% agarose gel.

Generation of E-cadherin knock-in cell lines

Epithelial BG1 cells were grown in a 12-well plate (150′000 cells/well) for 24h and cotransfected using 4 μL of ViaFect with 0.6 μg of hCas9, 0.2 μg of sg-A, 0.6 μg of double-cut NH donor_EGFP and 0.2 μg of CDH1_-60 or CDH1_-171 or CDH1_STOP in serum free-media. After 20 min of incubation, the reaction was added to the cells. Medium was changed 24h after transfection, cells were expanded and sorted for the EGFP positive population (He et al., 2016).

Patient-derived OC sample dissociation

Patient samples were cut with a scalpel in a petri dish as small as possible, placed in a 50 mL tube with digestion mix (5 mL RPMI with 10% FBS, 5 mL Accutase, 100 μL Collagenase and 3 μL DNAse I (2000 U/mL)) and incubated at 37°C, 200 rpm for 1 h. The tube was filled with PBS and centrifuged at 1100 rpm for 10 min. The supernatant was removed and the pellet resuspended in 20 mL PBS, filtered through a 70 μm cell strainer into a new 50 mL tube and centrifuged as before. After centrifugation, the supernatant was removed, red blood cell lysis (Miltenyi Biotec) was applied for 5–10 min and the tube filled again with PBS. After centrifugation (1500 rpm, 5 min), the supernatant was removed, the pellet was resuspended and the cells were counted for subsequent flow cytometry experiments.

Flow cytometry analysis

Cell surface GSL expression was analysed by flow cytometry (Cytoflex, Beckman Coulter, USA) after antibody labelling. Cells were grown to 80% confluency and harvested using a 1× non-enzymatic cell dissociation buffer (Sigma-Aldrich). Briefly, cells were washed in 96 well plates using FACS-wash (FW-1% BSA in PBS), incubated with the first GSL-binding antibody for 1 h at 4°C, washed 3 times with FW followed by incubation for 1 h with the secondary antibody. Finally, stained cells were washed 3 times and incubated with Streptavidin-FITC for an additional 30 min at 4°C. All investigated cell lines were gated individually to exclude debris, doublets or DAPI^{+} cells. Data analysis was performed using FlowJo v10 BD (Becton Dickinson, USA).

In vivo xenografts using zebrafish embryos

Animal experiments and zebrafish husbandry were approved by the ''Kantonales Veterinäramt Basel-Stadt''. *ΔST8SIA1* and parental cells were labelled with the fluorescent CellTracker CM-Dil. Transparent zebrafish were maintained, collected, grown and staged in E3 medium at 28.5°C according to standard protocols (Krauss et al., 2013). For xenotransplantation experiments, zebrafish embryos were anaesthetised in 0.4% tricaine (Sigma-Aldrich) at 48h post fertilisation and 75–100 human ovarian cancer cells were microinjected into the vessel-free area of the yolk or the zebrafish common cardinal vein (Duct of Cuvier) of a transgenic Tg(kdrl:eGFP) line, respectively. Embryos were incubated for 1 h at 28.5–29°C for recovery and then screened for the presence of fluorescent human cancer cells in the yolk (in case of yolk injection) or for the presence of cells in the tail (in case of injection into the Duct of Cuvier). Fish harbouring red cells were incubated at 35°C. Three days after transplantation, embryos were screened microscopically for tumour formation, extravasation, and secondary tumour mass formation using Leica TCS SP5 confocal microscope. For each experiment, 75–100 cells per fish were transplanted and at least 5 fish for each condition were analysed in multiple biological replicates.

Multiplexed capillary gel electrophoresis coupled to laser-induced fluorescence detection (xCGE-LIF)

Glycosphingolipids were analysed according to the standard protocol (Rossdam et al., 2019). Briefly, cells were grown at 90% confluency and 1.3×10^6 cells were harvested using non-enzymatic cell dissociation, pelleted through centrifugation, washed twice with PBS and frozen at −80°C. The cell pellets were resuspended in 1 mL chloroform/methanol (1:2, v/v), sonicated at 50% output in an ultrasonic bath for 15 min. After centrifugation for 5 min at 3000 rpm, supernatants were transferred into a large glass vessel. The extraction was repeated twice using chloroform/methanol (2:1, v/v) and chloroform/methanol (1:1, v/v). The different extraction supernatants were pooled and dried under nitrogen gas. Following this extraction, glycolipids were resuspended in chloroform/methanol (1:1, v/v) and desalted using pre-equilibrated (5mL H_2O) Chromabond C18 propylene columns and eluted with methanol. GSLs were treated with LudgerZyme Ceramide Glycanase (CGase) (Ludger, Oxfordshire, UK) in LudgerZyme Ceramide Glycanase RXN

buffer for 24h at 37°C and then mixed with 2 μL of 8-Aminopyrene-1,3,6-trisulfonic acid trisodium salt (APTS, 20 nM in 3.5 M citric acid), 2 μL of 2-picoline borane complex (PB, 2M in DMSO, Merck) as a reducing agent and 2 μL of water. The mix was incubated for 16.5h at 37°C in the dark. The reaction was stopped by adding 100 μL of acetonitrile/water (80:20). Excess of APTS and agents were removed by HILIC-SPE. Finally, labeled glycans were eluted, dried and analyzed using xCGE-LIF, Biosystems™ (ThermoFisher Scientific, Foster City, CA). Glycans were annotated using our in-house migration time database. Quantification was performed based on relative fluorescence signal intensities. Relative fluorescence signal intensities were calculated for individual peak intensities (heights) in relation to the sum of all peak intensities. Each cell line was analysed in triplicates derived from different passages.

DigiWest

Cells were lysed in 1× radioimmunoprecipitation assay buffer (RIPA, Cell Signalling Technology) containing proteinase inhibitor cocktails (Sigma-Aldrich). Lysates were clarified by centrifugation at 18,000 g for 15 min at 4°C. Clarified lysates were boiled in 1× sample buffer (50 mM Tris-HCl, 1% SDS, 100 mM DTT and 10% glycerol) at 95°C for 5 min and resolved by SDS-PAGE. DigiWest assays were performed as published (Treindl et al., 2016). For analysis 15 μg of cellular protein was loaded on a sodium dodecyl sulphate-polyacrylamide gel and size-separated by electrophoresis. The size-separated proteins were blotted to a polyvinylidene fluoride membrane and biotinylated on the membrane using NHS-PEG12-Biotin (50 μM) in phosphate-buffered saline (PBS) supplemented with 0.05% Tween-20 for 1 h. After drying of the membrane, the sample lanes were cut into 96 strips of 0.5 mm width, each corresponding to a defined molecular weight fraction. Each of the strips was placed in a well of a 96-well plate and a 10 μL elution buffer (8 M urea, 1% Triton X-100 in 100 mM Tris-HCl pH 9.5) was added. The eluted proteins were diluted with 90 μL of dilution buffer (5% BSA in PBS, 0.02% sodium azide, 0.05% Tween 20) and each of the protein fractions was incubated with 1 distinct magnetic colour-coded bead population (Luminex, Austin, TX, USA) coated with neutravidin. The biotinylated proteins bind to the neutravidin beads in such a way that each bead colour represents proteins of one specific molecular weight fraction. All 96 protein-loaded bead populations were mixed, resulting in a reconstitution of the original lane. Such a bead mix was sufficient for about 100 individual antibody incubations. Aliquots of the DigiWest bead-mixes (about 1/100th per well) were added to 96-well plates containing 50 μL assay buffer (Blocking Reagent for ELISA (Roche, Rotkreuz, Switzerland) supplemented with 0.2% milk powder, 0.05% Tween 20 and 0.02% sodium azide) and different diluted antibodies were added to the wells. After overnight incubation at 15°C in a shaker, the bead-mixes were washed twice with PBS containing 0.05% Tween 20, and PE-labelled (phycoerythrin) secondary antibodies (Dianova, Hamburg, Germany) were added and incubated for 1 hour at 23°C. The beads were washed twice prior to readout on a Luminex FlexMAP 3D instrument (Luminex, Austin, TX, USA).

For the quantification of antibody-specific signals, an Excel-based analysis tool was used that identifies peaks of appropriate molecular weight and calculates the peak area (Treindl et al., 2016). The intensity of the signal was normalised to the total amount of protein loaded into one lane.

Mass spectrometry based phosphoproteomics analysis

Wildtype, ⊿ST8SIA1 and ⊿A4GALT cancer cells were cultured in RPMI-1640 with 10% FBS. Cells were grown to 90% confluence and harvested using a lysis buffer (8M Urea, 0.1M ammonium bicarbonate, phosphatase inhibitors, 5 mM TCEP). Briefly, cells were washed two times with PBS and resuspended in 80 μL of lysis buffer, vortexed for 10 s, sonicated using Bioruptor®Pico (Diagenode) (30 s on, 30 s off, 10 cycles = 10 min), rotated 60 min (37°C, 1'400 rpm) and spun down (10 min, 10'000 rpm). For protein digestion, 1 μL of 0.75 M chloroacetamide solution was added to 200 μg of total protein and kept at 37°C for 30 min at 500 rpm. Samples were diluted with 320 μL of 0.1 M ammonium bicarbonate buffer and porcine trypsin (0.4 μg/μL stock) was added with a final enzyme/protein ratio of 1:50 (w/w) and digested overnight at 37°C. The next day, 100 μL of 5% TFA (Pierce/Thermo) was added and the samples purified using 2 times pre-equilibrated (500 μL of 0.1% TFA) C18 columns. Samples were loaded two times, spun down (1800 rpm, 30 s), washed three times with 500 μL of buffer C (5% acetonitrile/95% water (v/v) and 0.1% TFA), eluted two times using buffer B (50% acetonitrile/50% water (v/v) and 0.1% TFA), dried using vacuum and dissolved in 160 μL of the loading buffer (80% ACN, 0.1% TFA). Each cell line was analysed in triplicate at different passages.

Peptide samples were enriched for phosphorylated peptides using Fe(III)-IMAC cartridges on an AssayMAP Bravo platform (Agilent, Basel, Switzerland) according to the manufacturer's instructions. Chromatographic separation of peptides was carried out using an EASY nano-LC 1200 system (Thermo Fisher Scientific), equipped with a heated RP-HPLC column (75 μm × 36 cm) packed in-house with 1.9 μm C18 resin (ReproSil-Pur C18–AQ, 1.9 μm resin; Dr. Maisch GmbH). Aliquots of 0.75 μg total peptides were analysed per LC-MS/MS run at a flow rate of 200 nL/min. Mass spectrometry analysis was performed using an Orbitrap Fusion Lumos Tribrid Mass Spectrometer equipped with a nanoelectrospray ion source (Thermo Fisher Scientific). The acquired raw-files were imported into the Progenesis QI software (v2.0, Nonlinear Dynamics Limited). Quantitative analysis results from label-free quantification were processed using the SafeQuant R package v.2.3.2. (https://github.com/eahrne/SafeQuant/) to obtain peptide relative abundances. This analysis included global data normalisation by equalising the total peak/reporter areas across all LC-MS runs, data imputation using the knn algorithm, summation of peak areas followed by calculation of peptide abundance ratios. Only isoform-specific peptide ion signals were considered for quantification. The summarised peptide expression values were used for statistical testing of differentially abundant peptides. Here, empirical Bayes moderated t-tests were applied using a limma package (http://bioconductor.org/packages/release/bioc/html/limma.html). Heatmap analysis of KEGG hsa04510:focal adhesion pathway phosphoproteins and the KEGG pathview package were analysed using Pathview: An R/Bioconductor package for pathway-based data integration and visualisation.

Reactome pathway enrichment analysis

Proteomics identified differentially expressed proteins (FDR <1%) with ($\log_2 FC > 1$ or < -1 and p-value < 0.05) in knockout cells which were selected for the pathway enrichment analysis. The R ReactomePA package was applied to calculate the Reactome pathway enrichment (Yu and He, 2016).

Proliferation assay

A total of 1′500 cells in 200 l culture media was seeded into 96-well plates and the MTT-assay was performed daily up to 7 days after seeding: 20 μl of MMT-dye dissolved in PBS (Sigma-Aldrich) was added to the cells (final concentration: 0.5 mg/mL). After 3h, the medium was removed and the purple crystals were dissolved with 200 ul of DMSO. The optical density (OD, absorbance at 540 nm) was measured with a SynergyH1 Hybrid Reader (Biotek, Zurich, Switzerland). The data (mean ± SD of at least 6 independent experiments with different passages) are presented as relative proliferation as a function of time after seeding.

Anchorage independent growth

A base layer of 0.6% agar was prepared for each well from a 6 well plate. After polymerization, cells (10′000 cells) were harvested, filtered and resuspended in 0.4% agar solution on top of the base layer. Two weeks after seeding, colonies were fixed and stained using 1 mL of 4% formaldehyde and 0.05% crystal violet during 1 h. Finally, the agar was washed with milliQ water as often as needed and pictures were taken.

Anchorage dependent growth

Cells were harvested and seeded at a density of 300 cells per well in a 6 well plate. After 10 days of culture, cells were washed with PBS, fixed and stained with 1 mL of 4% formaldehyde and 0.05% crystal violet during 1 h and washed again with water

Migration assay

Cell lines (7.5×10^5 cells) were harvested using non-enzymatic cell dissociation (Sigma) and washed three times using RPMI-1640 growth medium. Cells were seeded in 500 μL of RPMI-1640 growth medium without FBS into the upper chamber of each insert. Cells were incubated for 24h and attracted by RPMI-1640 with 10% FBS (chemo-attractant) found in the lower part of the well. After incubation, growth media in the insert was removed and the lower side of the insert was stained with 4% formaldehyde and 0.05% crystal violet for 30 min. The insert was washed with milliQ water and the non-migrated cells were removed with a cotton-swab. Images (n = 4) were acquired to cover the entire insert with Olympus IX81 and the number of migrated cells was counted using Fiji.

Immunofluorescence staining and imaging

OC cells were grown on 8-well tissue culture chamber slides (Sarstedt, Switzerland) for up to 24 h, fixed with 4% paraformaldehyde, and rinsed three times in PBS for 5 min each. Once fixed, Alexa Fluor® 647 Phalloidin (Cell Signaling Technology) was diluted 1:20 (5 μL per 100 μL assay volume) in PBS and added to the cells. Slides were incubated for 15 min at room temperature, rinsed once with PBS, and cells were embedded in ProLong® Gold antifade reagent with DAPI (Cell Signaling Technology). Fluorescence images were taken by a Nikon CSU-W1 spinning-disk confocal microscope (Nikon Europe, Netherlands).

Immunoblotting

Cells were lysed in 1× radioimmunoprecipitation assay buffer (RIPA, Cell Signaling Technology) containing proteinase inhibitor cocktails (Sigma-Aldrich). Lysates were clarified by centrifugation at 18,000 g for 15 min at 4°C. Clarified lysates were boiled in 1× sample buffer (50 mM Tris-HCl, 1% SDS, 100 mM DTT and 10% glycerol) at 95°C for 5 min and resolved by SDS-PAGE. Proteins were then transferred to a polyvinylidene difluoride (PVDF) membrane (BioRad) and blocked with 5% (w/v) bovine serum albumin in TBST (20 mM Tris-Base, 150 mM NaCl, pH 7.8, 0.1% Tween 20) for 1 h at room temperature. The membrane was incubated with one of the listed primary antibodies diluted in 5% (w/v) BSA in TBST overnight at 4°C. After washing (3 times, 10 min) in TBST, the membrane was incubated with corresponding HRP-conjugated secondary antibodies (1:10000, Cell Signaling Technology) for 3h at room temperature. Finally, the membrane was developed using the Super Signal West Dura Extended Duration Substrate (Thermo Fisher Scientific) for detection of HRP. Western blot results were visualised by Gel Doc XR +™ (BioRad) and analysed by Image Lab™ software (BioRad).

QUANTIFICATION AND STATISTICAL ANALYSIS

Apart from the already described analysis above, statistical analysis and figures were obtained through the use of the software R Studio version 4.0.3 (www.R-project.org). All experiments were performed at least in triplicates and statistical evaluation was done using student's t tests, p-values of <0.05 were considered statistically significant (***, p < 0.001; **, p < 0.01; and *, p < 0.05). All data including error bars are presented as mean ± SD. Beside R/Bioconductor, remaining statistical

calculations were performed using GraphPad Prism 9.0. Two independent experimental groups were compared by using unpaired student's t tests.

Length and circularity of the cells were analysed using Cell segmentation with the region of interest (ROI) using polygon with QuPath to highlight the difference in cell morphology between our knockout cell lines. Cell size, cell length, and circularity were measured by cell segmentation using CellPose with cyto as a model and 120 pixels for the diameter (1 pixel represents 0.5 μm) and the analysis was processed by QuPath v0.2.0. Illustrations were created with BioRender.